Phosphorescent Cationic Heterodinuclear Ir III /M I Complexes (M=Cu I , Au I) with a Hybrid Janus-Type N-Heterocyclic Carbene Bridge

Anna Bonfiglio, Lenka Pallova, Vincent César, Christophe Gourlaouen, Stéphane Bellemin-laponnaz, Chantal Daniel, Federico Polo, Matteo Mauro

▶ **To cite this version:**

Anna Bonfiglio, Lenka Pallova, Vincent César, Christophe Gourlaouen, Stéphane Bellemin-laponnaz, et al.. Phosphorescent Cationic Heterodinuclear Ir III /M I Complexes (M=Cu I , Au I) with a Hybrid Janus-Type N-Heterocyclic Carbene Bridge. Chemistry - A European Journal, 2020, 26 (51), pp.11751-11766. 10.1002/chem.202002767 . hal-02937859

HAL Id: hal-02937859
https://hal.science/hal-02937859

Submitted on 12 Nov 2020

HAL is a multi-disciplinary open access archive for the deposit and dissemination of scientific research documents, whether they are published or not. The documents may come from teaching and research institutions in France or abroad, or from public or private research centers.

L'archive ouverte pluridisciplinaire **HAL**, est destinée au dépôt et à la diffusion de documents scientifiques de niveau recherche, publiés ou non, émanant des établissements d'enseignement et de recherche français ou étrangers, des laboratoires publics ou privés.

Phosphorescent cationic heterodinuclear Ir^{III}/M^{I} complexes (M = Cu^{I}, Au^{I}) with a hybrid Janus-type N-heterocyclic carbene bridge

Anna Bonfiglio,[a] Lenka Pallova,[b] Vincent César,[b] Christophe Gourlaouen,[c] Stéphane Bellemin-Laponnaz,[a] Chantal Daniel,[c] Federico Polo,[d] and Matteo Mauro*,[a]

Abstract: A novel class of phosphorescent cationic *hetero*bimetallic Ir^{III}/M^{I} complexes, where M^{I} = Cu^{I} (**4**) and Au^{I} (**5**), is reported. The two metal centers are connected by the hybrid bridging 1,3-dimesityl-5-acetylimidazol-2-ylidene-4-olate (**IMesAcac**) ligand that combines both a chelating acetylacetonato-like and a monodentate N-heterocyclic carbene site coordinated onto an Ir^{III} and a M^{I} center, respectively. Complexes **4**–**5** have been prepared straightforwardly by a stepwise site-selective metalation with the zwitterionic [(IPr)M^{I}(IMesAcac)] metalloproligand (IPr = 1,3-(2,6-diisopropylphenyl)-2*H*-imidazol-2-ylidene) and they have been fully characterized by spectroscopical, electrochemical and computational investigation. Complexes **4**–**5** display intense red emission arising from a low-energy lying excited state that is located onto the "Ir(C^N)" moiety featuring an admixed triplet ligand centered/metal-to-ligand charge transfer (^{3}IL/^{1}MLCT) character. Comparison with the benchmark mononuclear complexes reveals negligible electronic coupling between the two distal metal centers at the electronic ground state. The bimetallic systems display enhanced photophysical properties in comparison with the parental congeners. Noteworthy, similar nonradiative rate constant has been determined along with a two-fold increase of radiative rate, yielding brightly red-emitting cyclometallating Ir^{III} complexes. This finding is ascribed to the increased MLCT character of the emitting state in complexes **4**–**5** due to the smaller energy gap between the ^{3}IL and ^{1}MLCT manifolds, which mix via spin-orbit coupling.

[a] A. Bonfiglio, Dr. S. Bellemin-Laponnaz, Dr. M. Mauro
Institut de Physique et Chimie des Matériaux de Strasbourg, UMR7504
Université de Strasbourg, CNRS
23 rue du Loess, 67000 Strasbourg (France)
E-mail: mauro@unistra.fr
Homepage: *http://www.ipcms.unistra.fr/?page_id=31293*

[b] L. Pallova, Dr. V. César
LCC-CNRS UPR8241
Université de Toulouse, CNRS, Toulouse, France

[c] Dr. C. Gourlaouen, Dr. C. Daniel
Laboratoire de Chimie Quantique
Institut de Chimie de Strasbourg UMR7177
Université de Strasbourg-CNRS
4 Rue Blaise Pascal, 67000 Strasbourg (France)
E-mail: cgourlaouen@unistra.fr; c.daniel@unistra.fr

[d] Dr. F. Polo
Department of Molecular Sciences and Nanosystems
Ca' Foscari University of Venice
Via Torino 155, 30172 Venezia (Italy)

Supporting information for this article is given via a link at the end of the document.

Introduction

Among phosphorescent organometallic compounds, cyclometalated Ir^{III} complexes have proven to be an outstanding class of emitters with real-market application in efficient organic light-emitting diodes (OLEDs).[1] In such compounds, the presence of the heavy atom induces large spin-orbit coupling (SOC, constant ζ_{Ir} = 3909 cm^{-1}) effects and enable fast population of the lowest-lying triplet manifold that subsequently decays radiatively with high efficiency. Therefore, these emitters often display high photoluminescence quantum yields (PLQY), microsecond-long emissive excited states and tunable emission over the visible spectrum and beyond.[2] Recent studies, either purely theoretical or combining experiments with computational investigations, have taken part in the elucidation of the origin of luminescent properties in this class of molecules pointing to the fundamental role exerted by relativistic, such as SOC, and structural effect.[3]

To date, fine modulation of both redox and photophysical properties have been mainly achieved by judicious molecular design and control of the geometry and isomerization linkage of the coordinated ligands around the Ir^{III} center that selectively operate onto both the topology of the potential energy surfaces and electron density reorganization. Hence, a colorful palette of homo- and heteroleptic cyclometalated Ir^{III} complexes has been obtained when this metal center is combined with mono-, bi- and tri-dentate scaffolds. Surprisingly, major efforts have been devoted to studying monometallic species.

Photoactive *multi*-metallic systems have been matter of intense studies as well, typically involving Ru^{II} donors and either Os^{II} or Re^{I} acceptors connected through (poly)-pyridyl ligands.[4] Briefly, in these systems the photophysical output depends on the nature of the connecting scaffold. When insulating bridges have been employed, electronic communication between the metal centers has been found to be weak. Thus, each photoactive metal center retained the excited state properties of the parental, isolated, species and the multi-component system is typically characterized by (vectorial) photo-induced energy and/or electron transfer processes, which funnels the excitation energy onto the lowest-lying excited state. On the other hand, when the metal centers share the same heteroaromatic ligand, a certain degree of electronic coupling could be observed along with a sizeable perturbation of the excited state properties.

As far as Ir^{III} complexes are concerned, Balzani and co-workers authored the pioneering work describing homodinuclear Ir^{III} system connected via a 3,5-*bis*(pyridin-2-yl)-1,2-4-triazole[5]. Other groups investigated the effect of the introduction of longer π-conjugated spacers into either homo or heteronuclear structures as well, such as (oligo-)-*p*-phenylene bridges,[6]often

acting as an insulating ligand as well as phenylene-*bis*-ethynylene,[7] arylesters,[8] and diynes[9].

More recently, diiridium species connected through smaller ligands have gained increased attention sometimes featuring emissive properties that are comparable or even outperforming mononuclear counterparts.[10] This is because the presence of a second heavy metal center in close proximity could introduce manifold advantages, such as *i*) additional degree of freedom in fine tuning the coordination environment and, thus, redox and optical properties; *ii*) increased structural rigidity and chemical stability, which render less accessible nonradiative channels and *iii*) enhanced SOC that, in turn, enables larger values for the radiative rate constant, k_r. Therefore, a judicious design of poly-metallic species might afford compounds with enhanced optical properties.

Chloro-bridged iridium dimers are ubiquitous precursors for the synthesis of highly emissive mononuclear complexes, but they typically display poorer emission compared to mononuclear counterparts. For this reason, their investigation has been often overlooked. A few examples of dinuclear *bis*(μ-Cl) and *bis*(μ-NCO) dimers bearing fluorenylpyridine chromophoric ligand were described by Bryce,[11] displaying photophysical properties also suitable for OLED device fabrication. The same group expanded upon by introducing non-innocent hydrazide bridging ligands into diiridium complexes yielding systems with remarkable PLQY, high OLED performances and ground state metal-metal electronic communication[12] In addition, whilst fluorinated arylhydrazide bridging ligands promoted intramolecular π-π interaction leading to a sizeable decrease of the nonradiative rate constant, k_{nr} as well as improvement of PLQY and device stability;[13] the concomitant introduction of 1,2-diarylimidazole as the chromophoric cyclometalating ligands allowed to further push the emission wavelength into the sky-blue region with high efficiecy.[14] Moreover, oxamidato bridging ligands were found to favour electronic communication between the two iridium centers and yield highly efficient emitters with remarkably short excited state lifetime attributed to the improved SOC effect exerted by the bimetallic system.[15] Chi and co-workers reported on sublimable diiridium systems containing bridging pyrazolate-based tridentate ligands that displayed sky-blue to green emission, PLQY close to unity and remarkable performances as emitters in OLED.[16] Taking advantage of the presence of two (potentially) coordinating N atoms, pyridazine and pyridimidine-based bridging ligands have been employed as *bis*-bidentate,[17] and *bis*-terdentate[18] bridging scaffold by Williams and Kozhevnikov yielding orange-red emitters with sometimes excellent emission properties attributable to the enhanced SOC effect. Zhou and co-workers also reported homodinuclear iridium complexes based on *bis*-bidentate phenylpyridazine bridges with good emission properties and electroluminescence efficiencies in the red region.[19]

Luminescent *hetero*metallic complexes containing an Ir^{III} center sharing the same bridging ligand are rare, also because their synthesis requires cumbersome multistep procedures. In particular, ligands' structure should be judiciously designed so that the site selective metalation is achieved while preserving the emission properties.

Williams and Kozhevnikov reported on a trimetallic Pt^{II}_2/Ir^{III} assembly consisting of two *bis*-terdentate pyrimidine-based ligands chelating onto the octahedral metal ion, showing improved photophysical properties.[20] At a second stage, the series was expanded upon yielding a bright tetrametallic Pt^{II}_3/Ir^{III} red emitter,[21] and a Pt^{II}_2/Ir^{III} system with good performances in light-emitting electrochemical cells.[22] Notably, an example of star-shaped $Au^{I}/Ir^{III}/Pt^{II}$ was reported, which featured a broadband emission arising from the partial energy transfer occurring between Ir^{III} and Pt^{II} centers.[23]

NHCs represent an important class of ligands that possess unique features, such as strong σ-donation and relatively weak π-acidity. They are able to engage into strong M–C bond, thus resulting in thermally and photochemically stable complexes.[24] Owing their versatility and peculiar features, they are ubiquitous ligands in organometallic chemistry,[25] playing pivotal role in the development of efficient catalysts,[26] phosphorescent emitters,[27] and functional materials[28]. In the recent years, polytopic NHCs capable of coordinating two or more metal centers have emerged as a novel class of ligands that would enable "cooperative effects" induced by the spatial proximity of the metal ions through, for instance, intermetallic electronic coupling. In this way, polymetallic systems with enhanced chemical, redox and optical properties are expected. Nonetheless, most of the poly-metallic NHC-bridged systems investigated to date show no or weak electronic coupling between metal centers, due to the poor d_M-p_L orbital overlap in the metal-NHC scaffold. Yet, a few rare exceptions are known.[29]

Although the subject of matter is still in its infancy, the main efforts in this field have been devoted to systems potentially suitable for tandem catalysis[26a,30] and functional materials.[31,28a] Instead, photoactive systems built upon metal centers that share a common N-heterocyclic carbene scaffold and investigation of the resulting effects onto their optical properties and electronic communication have been largely overlooked. The systems investigated to date are depicted in Scheme 1. Bielawski and co-workers reported on the first example of luminescent di-metallic system comprising two cyclometalated Ir^{III} fragments, namely $[Ir(ppy)_2]$ (ppy = 2-phenylpyridyl), interconnected via the symmetric Janus-type di-NHC scaffold 1,7-dimethyl-3,5-diphenylbenzobis(imidazolylidene).[32] Comparison with the monometallic analogue revealed lack of metal-metal electronic communication through the bridge in the dimetallic species. This latter displayed phosphorescence originated from the unperturbed $[Ir(ppy)_2]$ moiety, yet with slower k_r and faster k_{nr}, thus resulting in poorer emission efficiency. Peris and co-workers described a pyrene-decorated alkyl-N-substituted bis(imidazolylidene) scaffold employed as bridge in a series of homo-dimetallic systems comprising $[M^{I}(COD)Cl]$ ($M = Ir^{I}$, Rh^{I} and COD = 1,5-cyclooctadiene),[33] cyclometalated $[Pt^{II}(ppy)]$[34] and terdendate $[M^{II/III}(CNC)]$ (where $M^{II/III} = Pt^{II}$, Au^{III} and CNC = 2,6-diphenylpyridine) fragments. While the former example was not luminescent as expected, the two latter ones displayed very weak luminescence attributable to the pyrene core that was largely quenched by the presence of the heavy metal. The same group described a heterodimetallic Pt^{II}-Au^{III} species bearing a Y-shaped

tris-NHC scaffold that was weakly photoluminescent in polymer thin-film with emission attributable to the [Au^{III}(CNC)] fragment.

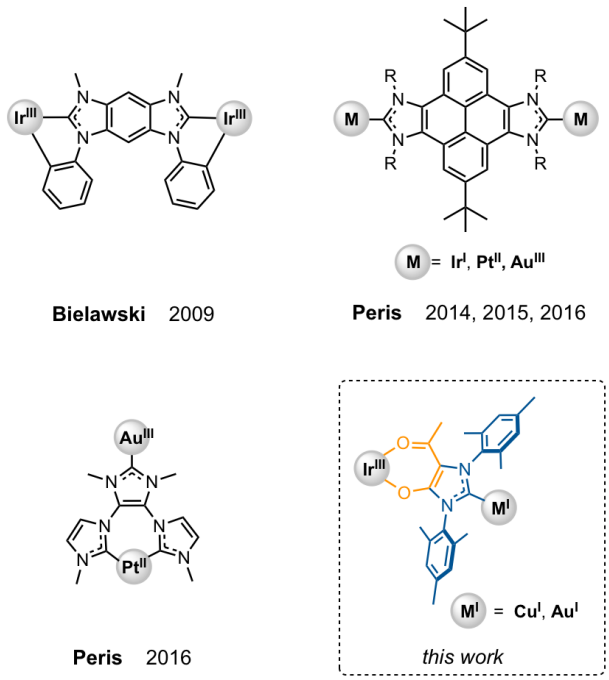

Scheme 1. Previous examples of photoactive bimetallic systems supported by bridging NHC scaffold and schematic representation of the Ir^{III}-M^{I} heterobimetallic systems supported by the hybrid **IMesAcac** ligand considered in this work.

Aiming at phosphorescent compounds with improved photophysical properties we therefore turned our attention onto multimetallic species. To the best of our knowledge, no paper reports on the optical properties of cyclometalated dimetallic systems bridged by a *hybrid* ambidentate NHC scaffold to date. This is in spite of the potential advantages that such skeleton might provide towards the construction of multimetallic functional systems. Herein, we report on a novel family of phosphorescent Ir^{III}/M^{I} complexes where the two metals are connected by the IMesAcac heteroditopic bridge (see Scheme 1). The binding ability of the “acac” site is selectively employed to chelate the luminescent [(C^N)$_2$Ir^{III}] moiety yielding a novel family of red-emitting Ir^{III} complexes with enhanced optical properties.

Results and Discussion

Synthesis

The **IMesAcac** ligand has been previously reported by César and Bellemin-Laponnaz[35] and features both an acetylacetonate-type and a diaminocarbene coordination sites. Both motifs are well known to be useful ligands largely employed for the construction of phosphorescent mononuclear complexes with remarkable optical properties based on Ir^{III}, Pt^{II}, Au^{I} and Cu^{I}. Therefore, the merge of both coordination sites onto one hybrid ligand renders the **IMesAcac** an ideal candidate for the preparation of emissive heterodinuclear species. On one hand, [Ir^{III}(C^N)$_2$] fragment has been chosen for the coordination onto the acac site of IMesAcac, owing to their superior emission properties. On the other hand, the [Cu(IPr)]$^+$ scaffold has been selected for the coordination onto the diaminocarbene site of the IMesAcac, because of its chemical and photochemical stability, linear coordination geometry, and its suitable optical properties (see below).

We prepared three different mononuclear complexes of general formula [Ir(κ^1C:κ^1N-C^N)$_2$(κ^2O,O-**IMesAcac**H)]PF$_6$ (**1**–**3**), where **IMesAcac**H is the protonated imidazolium precursor and C^N is the cyclometalating pro-ligand 2-phenyl-pyridine (ppy), 2-phenyl-benzotiazole (2-pbt) and 1-phenylisoquinoline (1-piq), respectively. We then investigated their optical properties to better select the most suitable candidate to be subsequently incorporated into the heterodimetallic species. The general synthetic pathway employed for the target complexes **1**–**3** is depicted in Scheme 2 and the chemical structures in Scheme 3. The dinuclear chloro-bridged Ir^{III} complexes [Ir(C^N)$_2$(μ-Cl)]$_2$ were used as the starting iridium compounds for the following reaction steps. They have been prepared by means of the classical Nonoyama reaction procedure.[36] The synthesis started with a halogen abstraction by using AgPF$_6$ as the silver(I) source in a slightly coordinating solvent, such as methanol, affording the corresponding *bis*-solvato complex of general formula [Ir(C^N)$_2$(MeOH)$_2$]$_2$. Upon removal of AgCl by filtration, the zwitterionic **IMesAcac**H was then added directly to the reaction mixture that was refluxed for 12 hours. Target mononuclear complexes **1**–**3** were obtained in purity suitable for photophysical investigation in moderate to good yield (44–87%) upon recrystallization. The formation of the desired complexes was supported by the lowering of the symmetry observed in the ^{1}H NMR spectra upon binding of the **IMesAcac**H ligand onto the Ir(C^N)$_2$ scaffold, which makes the protons onto the two cyclometalating ligand magnetically non-equivalent (see Figure S1–S3 and S6-S8 of the Supporting Information for full chemical characterization) Whereas, coordination through the pro-carbenic carbon can be ruled out due to the presence of the proton resonance at δ = *ca.* 8.9 ppm with singlet multiplicity corresponding to the NC(*H*)N proton of the imidazolium ring. Furthermore, the connectivity and crystallographic metrics were undoubtedly established by X-ray diffraction analysis for derivative **2** (*vide infra*).

It is worth to notice that the choice of both the solvent and reaction conditions are of crucial importance for the success of the synthesis. Indeed, any attempts to break the starting chloro-bridged dimer by direct addition of the **IMesAcac**H ligand in a solvent mixture more commonly used for similar reactions, such as a 3:1 CH_2Cl_2:MeOH,[37] yielded the starting materials unreacted. This results is in agreement with previous findings reported by César and Bellemin-Laponnaz.[38] In fact, the poor chelating ability of the acac moiety in the mesoionic **IMesAcac**H ligand make it unable to replace the chlorine ligand while reacted with the [(IPr)CuCl] motif. Abstraction of the bridging chlorine atoms with stoichiometric amount of AgPF$_6$ generated the solvato-complex [Ir(C^N)$_2$(solvent)$_2$]$_2$. Reaction of this latter with the **IMesAcac**H

ligand in CH_2Cl_2 resulted in the formation of the starting chloro-bridged dimer. Most likely, residual chloride anions compete efficiently with the weakly coordinating acac motif of **IMesAcac**H, even when the former is present in rather low amount. Moreover, the use of a more coordinating solvent, such as CH_3CN, left the corresponding starting material $[Ir(C^N)_2(solvent)_2]_2$ unreacted. Overall, these results confirm the weak coordination ability of the acac binding motif (*i.e.*, κ^2O,O) when associated to the cationic formamidinium moiety within the mesoionic **IMesAcac**H.[38]

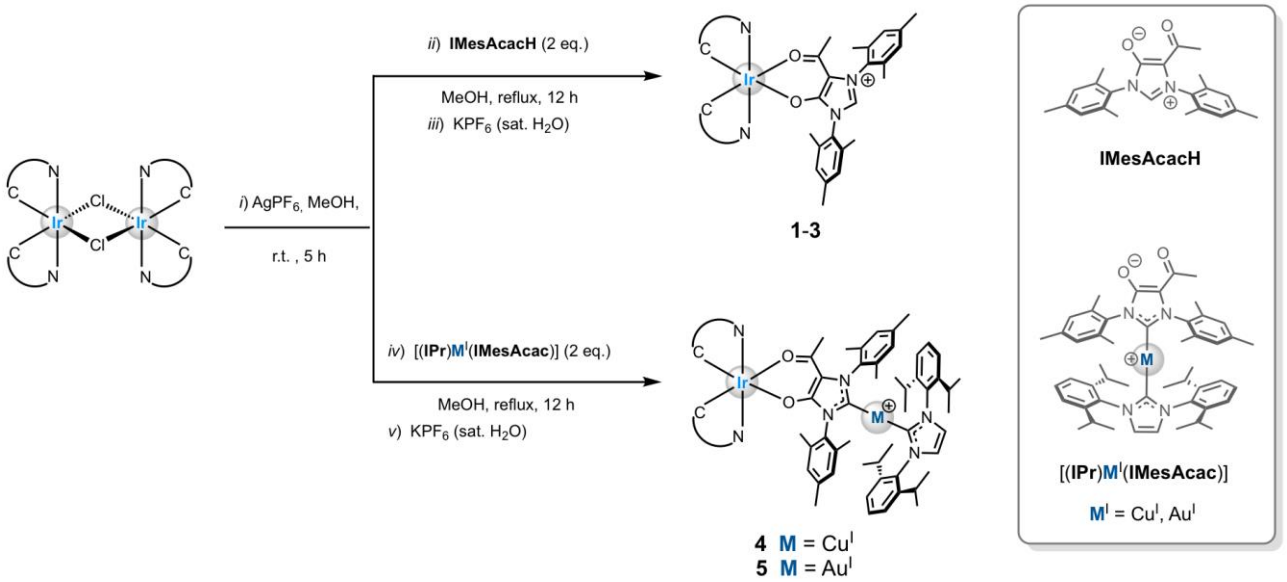

Scheme 2. Schematic synthetic pathway used for the synthesis of complexes **1**–**5**. All the complexes were prepared as PF_6^- salt.

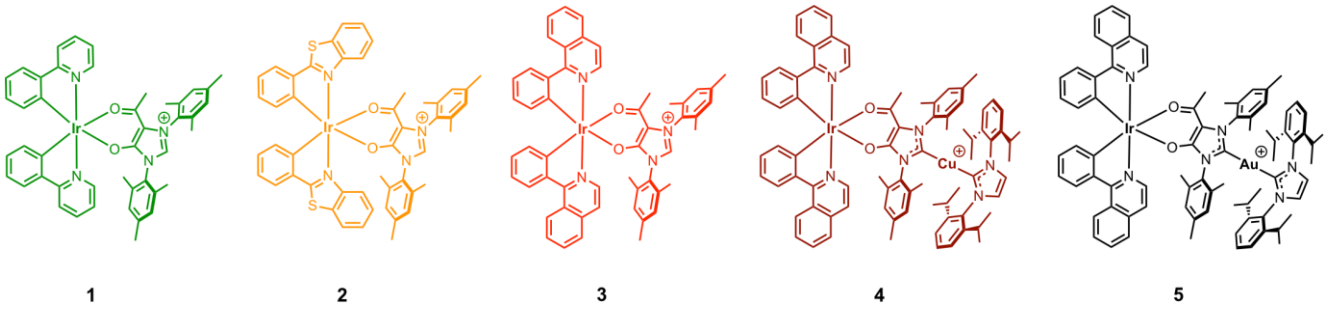

Scheme 3. Chemical structure of the investigated cationic complexes **1**–**5.**

Single crystals suitable for X-ray diffractometric analysis were obtained for complex **2** by slow diffusion of *n*-hexane into an acetone solution of the compound. The corresponding ORTEP diagram is shown in Figure 1 and refinement data are listed in Table S1 in the Supplementary Information. Complex **2** displays a slightly distorted octahedral geometry around the iridium center with the two cyclometalated ligands adopting a mutually eclipsed configuration. The X-ray structural characterization confirmed the *trans*-N,N coordination of the two phenyl-benzothiazole ligands with Ir–N distances lying at 2.044(2) and 2.048(2) Å for N(3) and N(4), respectively. The coordination sphere of the metal ion is completed by the **IMesAcac**H ligand that chelates through the acac-type coordination motif. As expected, slightly shorter bond distances are observed for the two Ir–C bonds with Ir–C(36) = 1.984(3) Å and Ir–C(49) = 1.992(3) Å, the latter residing to mutually *cis* locations. The slightly longer Ir–O distances in **2** [Ir–O(1) = 2.1703(19) Å, Ir-O(2) = 2.162(2) Å] relative to the ones observed within its benchmark analogue $[Ir(2\text{-pbt})_2(acac)]$ [Ir–O = 2.158(4) and 2.145(5) Å][39] reflect the poorer coordinating ability of the neutral I**MesAcac**H ligand *vs* a classical anionic acac ligand.

Figure 1. ORTEP diagram of compound **2** with thermal ellipsoids shown at 30% probability level obtained by single-crystal X-ray diffractometric analysis. All hydrogen atoms except the one on the pre-carbenic position, solvent and conter-anion are omitted for clarity. Selected bond lengths (Å): Ir–C(36) = 1.984(3) Å; Ir–C(49) = 1.992(3) Å; Ir–N(3) = 2.044(2) Å, Ir–N(4) = 2.048(2) Å, Ir–O(1) = 2.1703(19) Å; Ir–O(2) = 2.162(2) Å.

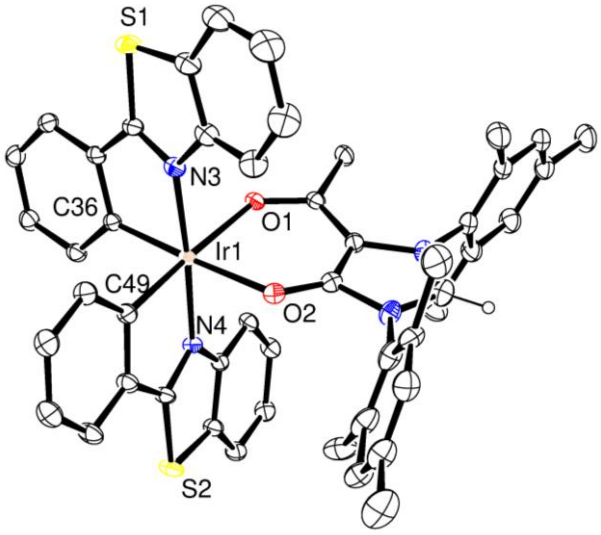

For the preparation of the heterodinuclear species, the "[Ir(1-piq)$_2$]" fragment was selected as the most suitable on the basis of the following grounds: *i*) computational analysis shows less mixing between the low-lying IL_{C^N}/$MLCT_{C^N}$ states and those involving the IMesAcac moiety (see below); *ii*) the parental complex **3** possesses the largest spectral separation with the **[(IPr)M^I(IMesAcac)]** species along the series **1**–**3**, thus allowing selective excitation into the lowest-lying ^{1}MLCT band located onto the „[Ir(1-piq)$_2$]" (see below); *iii*) complexes emitting into the red/near infrared portion of the electromagnetic spectrum typically display lower PLQY when compared to green and yellow emitters. This is beacause they possess typically slower k_r due to the ν^3 dependency of Einstein spontaneaus emission coefficent and faster k_{nr} due to energy gap law consideration.[40] Red emitters would then benefit the most from the favourable increase of the k_r.

The synthesis of the heterodinuclear complexes employed a stepwise site-selective metalation procedure that straighfowardly afforded the target Ir^{III}/M^I species (Scheme 2). Upon chloride abstraction using $AgPF_6$ onto the dichloro iridium dimer, the zwitterionic metalloligand that features an acac-type of coordination motif, namely M^I(κ^1*C*-IPr)(κ^1*C*-**IMesAcac**), is then added, yielding the target complexes **4** and **5** with M = Cu^I and Au^I, respectively, upon re-crystallization with an aqueous solution of KPF_6. The ^{1}H, ^{13}C and ESI-MS spectra are displayed as Supporting Information in Figure S4–S5 and S9–S10, respectively.

Photophysics

The photophysical properties of complexes **1**–**3** were investigated at concentration of 3.0×10^{-5} M in both air-equilibrated and degassed acetone solution at room temperature as well as in 2-methyltetrahydrofuran (2-MeTHF) glassy matrix at 77 K. The data are listed in Table 1 and the electronic absorption and photoluminescence spectra are displayed in Figure 2. The most intense transition present in the region λ_{abs} = 350–400 nm is confidentially attributed to spin-allowed ligand centered (^{1}IL) processes, although the complete profile of the band could not be recorded due to the limitation of the spectral window of the solvent employed. At lower energy, in the region λ_{abs} = 400–500 nm, the spectra feature broad and featureless transitions with moderate intensity ($\varepsilon \approx 2–6\times10^3$ M^{-1} cm^{-1}) that are partially overlapped. This band is ascribed to spin-allowed electronic processes with mainly metal-to-ligand charge transfer (^{1}MLCT) character as by comparison with related [Ir(C^N)$_2$(acac)] complexes reported previously[41] and based on computational investigations (see below). The weak band visible at an even longer wavelength (*e.g.*, λ_{abs} = 578 nm, $\varepsilon = 0.5\times10^3$ M^{-1} cm^{-1} for compound **3**) is assigned to the formally spin-forbidden ^{3}MLCT transition owing to the improved zero-field splitting exherted by the octahedral coordination enviroment imposed by the Ir^{III} atom.[42] A clear modulation of the absorption onset is observed in the series featuring a bathochromic shift in the order **1** to **2** to **3**, which parallels the increasing π-accepting ability of the N-containing heteroaromatic ring coordinated onto the iridium atom. A more detaiteld assignment based on TD-DFT calculations is provided in the section dedicated to the computational results.

Upon excitation in the ^{1}MLCT band, acetone samples of all the compounds display photoluminescence in both air-equilibrated and degassed condition. The corresponding normalized spectra are shown in Figure 2 and the data listed in Table 1. The emission spectra display a bathochromic shift going from **1** to **2** to **3** that parallels the trend observed in the absorption spectra. Surprisingly, air-equilibrated samples of complex **1** clearly show two broad and featureless emission bands centered at 520 and 655 nm and an overall PLQY as low as 0.05%. Instead, the former band dominates the emission profile upon degassing the sample and display a lifetime as long as 1.2 μs thus unambigously confirming the phosphorescence nature of the such high energy band (namely P_1) that is tentatively attributed to an emissive state with $^3MLCT_{ppy}$/$^3IL_{ppy}$ character, d(Ir)π(phenyl)←π*(pyridine), as by comparison with the parental [Ir(ppy)$_2$(acac)] complex.[41,43] Incorporation of a more extended π-system, such as either the benzothiazole ring or the isoquinoline moiety, onto the cyclometalating C^N ligand causes a shift of the emission to lower energies, being λ_{em} = 546 and 583 nm (**2**), and 607 and 650 nm (**3**), whose profile appear to be virtually independent of the presence of dioxygen. Nonetheless, increase of the PLQY from 1.9% to 3.5% (compound **2**) and from 2.5% to 18% (compound **3**) is observed, again pointing toward the triplet nature of the emissive excited state. Noteworthy, for compound **3** emission profile resembles closely that of the related complex [Ir(1-piq)$_2$(acac)] with PLQY value comparable within the experimental error.[44] The sizeable increase of the vibronic structure observed moving from compound **1** to **3** indicates that mixing between $^3MLCT_{C^N}$ and $^3IL_{C^N}$ occurs to a lower extent due to the more extended π-conjugation of the moiety involved in the radiative transition and agree well with the emission of the corresponding [Ir(C^N)$_2$(acac)] congeners.[41,43] Analysis of the excitation spectra recorded at both maxima for complexes **1** are displayed in Figure S11. The two excitation spectra show slightly different profile, also when compared to the absoption spectrum, corroborating the idea that the two emission bands originate from electronically uncoupled excited states. On the other hand, for

compound **2**–**3** the excitation spectrum recorded at the emission band maximum resembles closely the absorption spectral profile (see Figure S12–S13).

Time-resolved analysis of the photoluminescence of compounds **1**–**3** revealed interesting information. Indeed, the excited state kinetic data recorded in degassed condition required a fitting with bi-exponential model for the three compounds **1**–**3**. As an example, complex **3** displays two decays with τ_1 = 1.55 μs (62%) and τ_2 = 1.03 μs (38%) at λ_{em} = 610 nm, and τ_1 = 1.6 μs (51%) and 1.1 μs (49%) at λ_{em} = 660 nm, highligthing the presence of a triplet state (namely P_2) that is close in energy to the emissive $^3IL_{C^N}/^3MLCT_{C^N}$ characteristic of the "[Ir(1-piq)$_2$(acac)]" scaffold (P_1 state). Such P_2 state appears to be present in the three complexes of the series **1**–**3** and it is most likely at the origin of the band clearly observed at λ_{em} = 655 nm for complex **1**. To further elucidate the origin of such poorly emissive state, the energy of the ^{3}IL state located onto the **IMesAcac**H ligand was evaluated by recording the photoluminescence spectrum of the corresponding Gd^{III} complexes at low temperature at 77 K glassy matrix in 2-MeTHF (see Figure S16 of the Supporting Information). The spectrum displays an onset at λ_{em} = 436 nm (2.84 eV) on the high-energy side, which allowed us to confidentently rule out the π-π* nature localized onto the **IMesAcac**H ligand, namely $^3IL_{\mathbf{IMesAcac}H}$, of the P_2 band, being the former positioned to much higher in energy than the latter. Clearly, the broad and featureless profile of this latter points toward a ^{3}CT nature instead.

To further investigate the emissive properties and the origin of the lower energy band, low temperature (77 K) photoluminescence experiments were carried out for samples of **1**–**3** in 2MeTHF glassy matrix (Figure 3 and Table 1). In this condition complexes **1**–**3** display intense emission with highly vibronic profile and mono-exponential decay over the whole emission band resembling those of parental [Ir(C^N)$_2$(acac)] complexes, indicating that population of the P_2 band might occours through a thermally-activated process at room temperature.

Overall, P_2 band is tentatively attributed to a triplet ligand-to-ligand charge transfer character, namely $^3LLCT_{\mathbf{IMesAcac}H}$, with a metal perturbed C^N → **IMesAcac**H character, close-lying to the emissive $^3IL_{C^N}/^3MLCT_{C^N}$ (Figure 4). Indeed, going from compound **1** to **2** to **3**, the $^3LLCT_{\mathbf{IMesAcac}H}$ level is expected to be affected to a minor extent; whilst, the stabilitation of the $^3MLCT_{C^N}/^3IL_{C^N}$ provided by the more extented π-conjugation of the system increases the energetic barrier for the $P_1 \rightarrow P_2$ process, rendering the thermal population of the poorly emissive P_2 more difficult. This assigment is also in agreement with computational findings (see below).

The absorption and emission spectra of the hetero-dimetallic complexes **4–5** are shown in Figure 2 and the excitation spectra are displayed in Figure S14–S15. The data listed in Table 1. They feature an absorption spectrum at room temperature that almost traces out the one of the monometallic counterpart **3**, thus confirming the negligible electronic coupling between the two metal centers at the electronic ground state. Remarkably, going from **3** to **4**–**5** a small bathochromic shift is observed for the band attributable to the admixure of ^{1}MLCT and ^{3}MLCT transitions that involves the cyclometalating C^N and acac moiety ($\lambda_{abs,max}$ = 458 nm for **3** and and 465 nm for **4**–**5**). This attribution is in agreement with our computational investigations and also with those reported previously.[45] This finding corroborates the energetic stabilisation of the MLCT state in the dimetallic species.

The photoluminescence spectra of **4–5** are bathochromically shifted by 8 nm (215 cm^{-1}) in comparison with the parental compound **3.** The spectra show comparable vibronic progression with fundamental spacing of 1290 cm^{-1} and similar Huang-Rhys factor; the latter indicates that compounds **3**–**4** possess comparable vibronic coupling between the emitting T_1 and the S_0 state. In sharp contrast, the bimetallic species display mono-exponential excited-state decay kinetics and a twofold increase of PLQY (τ = 1.6 μs and PLQY = 36% in degassed acetone). One should notice that this value of PLQY are much higher than the benckmark complex [Ir(1-piq)$_2$(acac)][44] and amongst the highest for red-emitting cationic Ir^{III} complexes.

For sake of comparison, the absorption and photoluminescence spectra of the parental complexes [**(IPr)Cu(IMesAcac)**] and [**(IPr)Au(IMesAcac)**] were recorded in acetone solution under identical condition (see Figure S17 of the Supporting Information). Expectantly, the electronic absorption spectrum displays intense and narrow emission band in the UV region with an onset at λ_{abs} = *ca.* 380–385 nm for both complexes that can be attributed to a ^{1}IL transition. Upon photoexcitation at λ_{exc} *ca.* 340 nm, they both display a very weak, narrow and featureless emission with small Stokes shifts. In particular, for degassed samples of [**(IPr)Cu(IMesAcac)**] two bands are present, namely a higher and a lower energy bands with maximum centered at λ_{em} = 410 and 544 nm, respectively. Overall, these findings are in agreement with those reported previously for similar species.[27,46]

As far as the hetero-bimetallic species **4**–**5** are concerned, the presence of a second metal atom coordinated through the bridging ancillary ligand onto the "[Ir(1-piq)$_2$]" scaffold is expected to modify the excited state properties by eliminating the poorly emissive close-lying $^3LLCT_{\mathbf{IMesAcac}H}$ state. Moreover, closer look at the excited state kinetic parameters indicates that the presence of the second metal center, such as the [(IPr)M^I(IMesAcac)] moiety, onto the emissive "[Ir(1-piq)$_2$]" scaffold largely improves the photophysical properties of this latter. The origin of this result stems from a two-fold effect. A decrease of the k_{nr} is observed due to the absence of the $^3LLCT_{\mathbf{IMesAcac}H}$ state in the bi-metallic species, being k_{nr} = 4.0×10^5 s^{-1} and 6.1×10^5 s^{-1} for compounds **4**–**5** and **3**, respectively. Alongside, an almost two-fold enhancement of the radiative rate constant is determined, being k_r = 2.3×10^5 s^{-1} and 1.3×10^5 s^{-1} for **4**–**5** and **3**, respectively. The data obtained for compound **3** are in well agreement with those reported for "[Ir(1-piq)$_2$(acac)]" benchmark complex, k_r = 1.2×10^5 s^{-1} and k_{nr} = 4.8×10^5 s^{-1}.[44]

In general, the radiative rate of the transition between the T_1 and S_0 can be expressed as follows for a transition metal complex (eqn. 1):[47]

$$k_r \propto \overline{\nu}^3 \left| \sum_m \frac{\langle S_m | \hat{H}_{SO} | T_1 \rangle}{E_{T_1} - E_{S_m}} \cdot \langle S_0 | e\boldsymbol{r} | S_m \rangle \right|^2 \qquad eqn.\,1$$

where $\bar{\upsilon}$ is the electronic transition energy expressed in cm^{-1}, ***er*** is the electric dipole operator, the term $\sum_m \frac{\langle S_m|\hat{H}_{SO}|T_1\rangle}{E_{T_1}-E_{S_m}}$ in the squared brakets relates with the SOC matrix elements between the singlet S_m and the T_1 state, and the matrix element of the second term, $\langle S_0|\boldsymbol{er}|S_m\rangle$, represents the transition dipole moment of the spin-allowed transition between singlet ground state S_0 and the higher-lying S_m state, E_{T_1} and E_{S_m} is the energy of the T_1 and S_m state, respectively.

A closer analysis of the parameters influencing the k_r indicates that the bathochromic shift observed for **4**–**5** when compared to the parental complex **3** might instead yield a smaller k_r. In addition, contribution from an increased transition dipole moment of the ^{1}MLCT state from where the emitting state stems from has to be ruled out. Indeed, the low-energy side of the profiles of the molar extinction coefficient spectra nicely overlap for complexes **3**–**5**. Likewise, in the frame of an indirect SOC mechanism, the energy level of the unperturbed ^{3}IL should be similar for **3**–**5**. Instead, the HOMO level is expected to be destabilized by the stronger donating nature of the "acac" moiety in the bimetallic species **4**–**5** compared to the monometallic counterpart **3**, yielding a decrease of the ^{1}MLCT and, thus, a smaller energetic separation between the first-order perturbation mixing of the ^{1}MLCT and ^{3}IL states. This is in agreement with the computed values of the frontier orbitals as well as the experimetal electronic absorption spectra and oxidation potentials (*vide infra*).

Modulation of k_r via variation of the ancillary ligand has been previously reported,[45b,10-15] but their enhancement in heterometallic systems connected via the ancillary ligand is unprecedented, to the best of our knowledge.

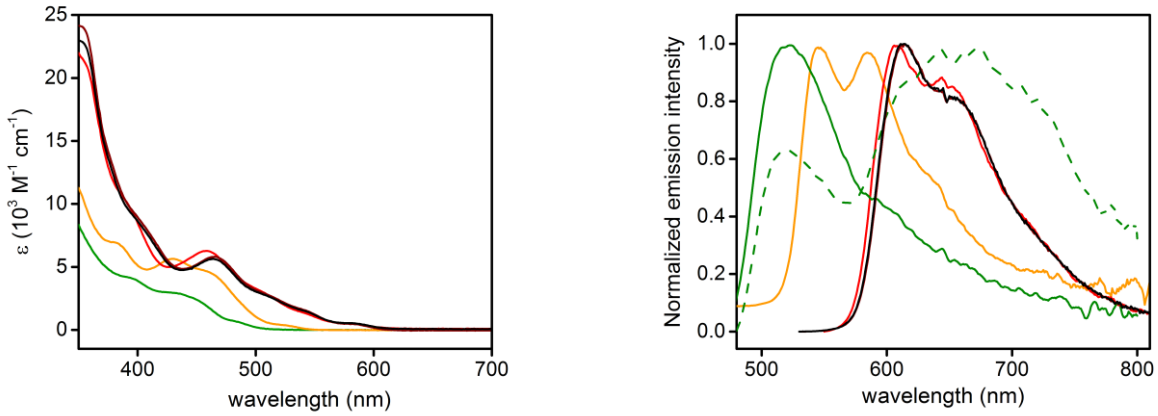

Figure 2. Electronic absorption (left box) and emission spectra (right box) for **1** (green trace), **2** (orange trace), **3** (red trace), **4** (dark red trace) and **5** (black trace) in acetone at concentration of 3.0×10^{-5} M in degassed condition. For sample of **1**, emission spectra of the air-equilibrated sample are shown as dashed trace. Samples were excited at λ_{exc} = 410, 450, 460, 470 and 460nm for compound **1**, **2**, **3**, **4** and **5**, respectively.

Table 1. Photophysical properties of complexes **1**–**5** recorded in air-equilibrated and degassed acetone solution at concentration of 3×10^{-5} M at room temperature and 77 K.

compound	$\lambda_{max,abs}$ (ε) [nm, (10^3 M^{-1} cm^{-1})]	λ_{em} [nm]	PLQY (%)		τ □μ□□		λ_{em} [nm]	τ □μ□□
			air-equilibrated	*degassed*	*air-equilibrated*	*degassed*	*77 K*	
1	395 (4.13), 440 (2.78), 482 (0.63)	520, 655	0.05	0.2	0.021[a,b] 0.019[c]	1.24[a,b] 1.37[a,d]	493, 530, 570	1.3[a]
2	383 (7.02), 428 (5.71), 459 (4.65), 522 (0.40)	546, 583, 640	1.9	3.5	89 ns	152 ns	532, 578, 628	3.8

3	390 (10.1), 458 (6.24), 502 (3.14), 540 (1.43), 578 (0.51)	607, 650	2.5	18	199 ns	1.35[a]	596, 645, 704	2.8
4	410 (8.10), 465 (5.77), 511 (2.85), 582 (0.63)	615, 655	3.5	36	165 ns	1.6	596, 645, 704	2.8
5	410 (7.37), 465 (5.67), 511 (2.65), 582 (0.60)	615, 655	3.7	36	170 ns	1.6	596, 645, 704	2.9
[Ir(1-piq)$_2$(acac)] [e]	–	622	–	20	–	1.7	–	–
[(IPr)Cu^I(IMesAcac)]	343 (17.6) 363 (9.69) 372 (2.00)	407, 539	-	-				
[(IPr)Au^I(IMesAcac)]	347 (21.2) 365 (11.5) 378 (2.00)	400, 534	-	-				

sh denotes a shoulder; [a] average lifetime (see experimental methods for details); [b] λ_{em} = 520 nm; [c] λ_{em} = 660 nm; [d] λ_{em} = 650 nm; [e] data from Ref. 44.

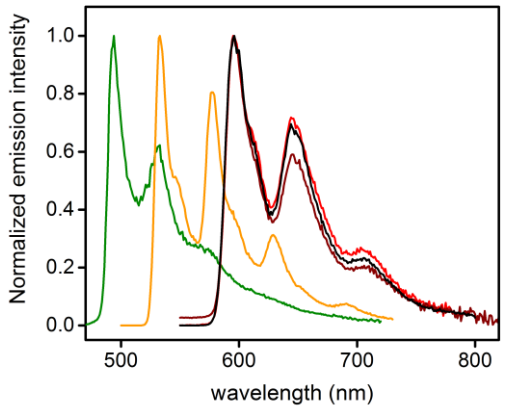

Figure 3. Emission spectra recorded for compound **1** (green trace), **2** (orange trace), **3** (red trace) and **4** (dark red trace) and **5** (black trace) in 2Me-THF glassy matrix at 77 K. Samples were excited at λ_{exc} = 400 nm for **1**–**2**, 420 nm for **3**, 450 nm for **4** and 460 nm for **5**.

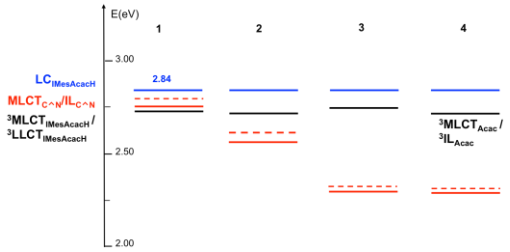

Figure 4. Schematic representation of the energy levels and nature of the low-lying excited states at Franck-Condon for the compounds **1**–**4** based on theoretical results (see next section Table 4) and experimental data for ^{3}IL$_{IMesAcacH}$.

Electrochemical characterization

The electrochemical behavior of compounds **1**–**4** was assessed by cyclic voltammetry (CV) in acetone/0.1 M tetrabutylammoniumhexafluorophosphate ($TBAPF_6$). All the electrochemical data are referenced against ferrocene/ferricenium couple as the internal standard and are reported in Table 2.

In the positive-going scan, all compounds **1**–**4** showed one main reversible oxidation process $O_{1,n}$, (with n denoting the compound number, namely **1**–**4**), whose standard potential E^o varied from +0.56 V to +0.82 V. Instead, in the negative-going scan, one or more irreversible and reversible reduction processes $R_{i,n}$ (where i denotes the process number and n the compound)

occurred in the potential range from –2.00 V to –2.90 V. Voltammetric investigations in the full width potential window are shown in Figure S18 in the Supporting Information. In Figure 5 the two main oxidation ($O_{1,1-4}$) and reduction ($R_{1,1-4}$) processes are shown to evidence the electrochemical HOMO–LUMO band gap. Moreover, to better appreciate the redox processes, cyclic voltammetries for both the positive- and negative-going scans were acquired separately and displayed in Figure 6. It is interesting to note that $O_{1,n}$, which is related to the oxidation of the iridium metal center, formally from Ir(III) to Ir(IV), with involvement of the cyclometalated phenyl ring, has a similar value for **1** and **3**, as the chelating ppy and 1-piq provide the metal center a similar electron-donating effect. On the other hand, the oxidation potential of **2** is shifted anodically by about 120 mV to reach +0.82 V. A similar observation has been previously reported in literature, although in that case the solvent was a 1:1 mixture of acetonitrile and 1,4-dioxane.[48]

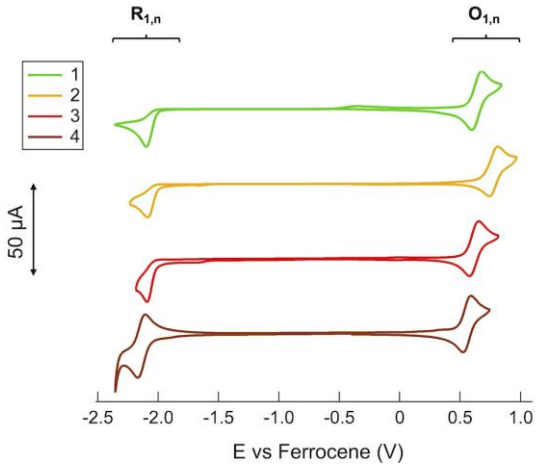

Figure 5. Background-subtracted cyclic voltammetries of 1 mM **1**–**4** in acetone/0.1 M $TBAPF_6$ at 0.2 Vs^{-1} for $O_{1,1-4}$ and $R_{1,1-4}$ processes.

Interestingly, the addition of a second metal center in **4**, namely a Cu^{I}, dramatically lowers the oxidation potential down to +0.56 V, thus pointing out that the HOMO is affected (*ca.* 80 mV with respect to **1** and **3**) by the presence of second metal center. This is due to the more donating ability of the acac moiety in the bimetallic species **4** than in the monometallic complex **3**, as previously shown in Ru^{II} complexes.[38] In the negative-going scan, **1**–**3** showed an irreversible process $R_{1,1-3}$ in the range from –2.04 V to –2.08 V, which was assigned to the reduction of the **IMesAcac**H ancillary ligand. In fact, **1**–**3**, which share the **IMesAcac**H as the chelating ligand, showed an almost overlapping $R_{1,1-3}$ process at an average potential value of –2.06 V. CV of **IMesAcac**H showed two irreversible peaks at +0.85 V and +1.20 V in the positive bias and one irreversible process in the negative bias at –2.82 V (see Figure S19). Indeed, the zwitterionic character of the free **IMesAcac**H ligand is lost when chelating the metal complex, leaving only a positive charge that makes the reduction easier of about 660 mV moving from –2.82 V to –2.06 V. On the other hand, the presence of a residual positive charge also suggests that its oxidation would be made more difficult, thus assuring that $O_{1,1-3}$ processes are solely due to the iridium metal center involving the cyclometalating N^C ligands. The positive residual charge is then localized on the copper center in **4**, which is instead characterized by a reversible process $R_{1,4}$ at –2.14 V, attributed to the reversible reduction of the cyclometalating 1-piq ligand. In fact, the CV of the monometallic parental complex [**(IPr)Cu(IMesAcac)**] (see Figure S20) revealed that no reduction process occurred even at potential lower than –2.50 V. Therefore, the reduction can be only due to 1-piq.

The effect of the scan rate was investigated over the range 50–500 mV s^{-1}, and the peak current was found to depend linearly with the square root of scan rate for all compound, thus witnessing that the heterogeneous electron transfer process is diffusion-controlled. On the other hand, the difference between the peak potential and the half-way peak potential, E_p-$E_{p/2}$, varied in the range of 40–70 mV for for $R_{1,n}$ regardless of the scan rate, while peak potentials shifted towards more negative potentials (by *ca.* 20 mV). These data are in agreement with the occurrence of a diffusion-controlled heterogeneous electron transfer reaction, followed by a very fast chemical reaction (EC process). It is worth noting that the ratio between the anodic peak current, $i_{p,a}$, for $O_{1,1-3}$ and the cathodic peak current, $i_{p,c}$, for $R_{1,1-3}$ is very close to unity for all the compounds, confirming that the processes are monoelectronic.[49]

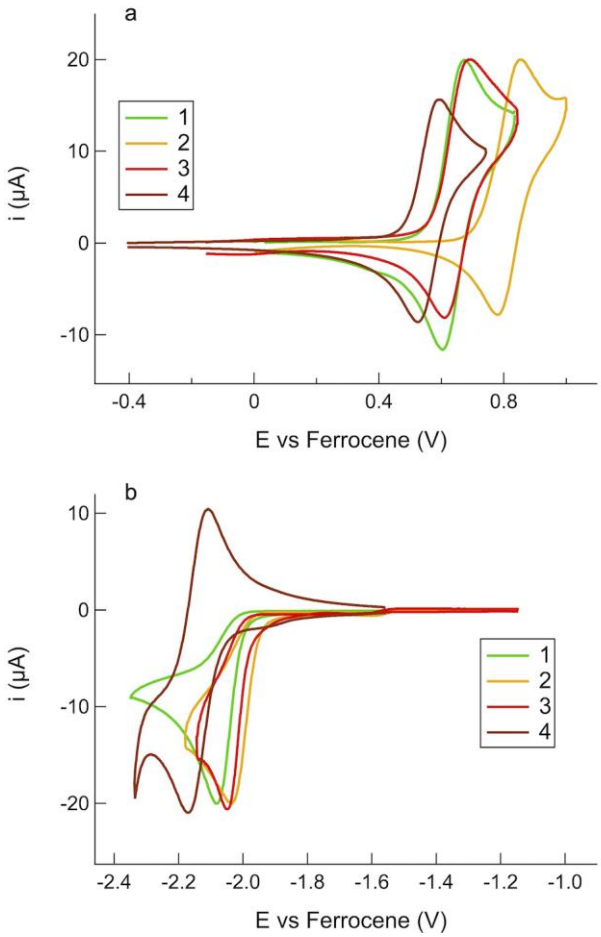

Figure 6. Background-subtracted CVs in the (a) positive- and (b) negative-going scan for 1 mM **1**–**4** in acetone/0.1 M TBAPF6 at 0.2 Vs^{-1}.

Following $R_{1,n}$ other processes appeared in the negative bias, as reported in Table 2 and shown in Figure S18, Supporting Information. Only for compound **1** those processes occurred close to the lower limit of the potential window and could not be determine precisely by CV. Therefore differential pulse voltammetry (DPV) was employed (see Figure S21). Instead, **2** and **3** showed a reversible wave ($R_{2,2\text{-}3}$) at –2.39 V and –2.57, which were attributed to the reduction of 2-pbt and 1-piq C^N ligand, respectively, followed by an irreversible one ($R_{3,2\text{-}3}$) at about –2.77 V. On the other hand, **4** featured two other irreversible processes, $R_{2,4}$ at –2.44 V and $R_{3,4}$ at –2.64 V. For the sake of clarity we also note that weak redox processes appeared in the anodic scan at about 0.40, 0, –0.50 and –1.20 V (see Figure S18) when scanning first cathodically and then reverting the scan direction. However, we did not investigate the nature of such processes, as they were beyond the scope of this work, except for the one occurring at about 0.40 V. With respect to **4**, it is interesting to note that, when a CV is carried out in the positive-going scan after the potential is kept at –2.50 V for 20 s an additional irreversible oxidation process appeared at +0.35 V ($O_{2,4}$), which is more likely due to the re-oxidation of **IMesAcac**H stripped away from the metal complex. A similar behavior was observed also for **1**-**3**.

Table 2. Electrochemical data for compound **1**–**4** obtained by cyclic voltammetry in acetone/0.1 M TBAP as the supporting electrolyte.

	$O_{i,n}$				$R_{i,n}$	
Cmpd *(n)*	$E^0(V)$ [a]	$\Delta E_p\ (mV)$ [b]	$E_p - E_{p/2}\ (mV)$ [b]	$i_{a,O_1}/i_{c,R_1}$ [c]	$E_{p,c}\ (V)$ [b]	$E_p - E_{p/2}\ (mV)$ [b]
1	+0.64	70	60	0.93	–2.08 –2.68 –2.87	50
2	+0.82	70	70	1.00	–2.04 –2.39 [a] –2.76	40 70
3	+0.65	70	60	1.05	–2.05 –2.57 [a] –2.77	42
4	+0.56 +0.35 [b,e] +1.44 [b]	70	60	0.80	–2.14 [a] –2.44 –.64	60
IMesAcacH	0.85 1.20		110 50		–2.82	70
[(IPr)Cu(IMesAcac)]	+0.33					

[a] $E^0_{O_{i,n}}$ or $E^0_{R_{i,n}}$ = average value between the anodic and cathodic peaks, calculated over a scan rate range 0.05-0.5 Vs^{-1}. [b] Measured at 0.2 Vs^{-1}. [c] Calculated at 0.2 Vs^{-1}. [d] Measured by DPV. [e] It appears only when scanning in the positive bias, once the potential is kept for 20 s at –2.5 V. All the potential values are reported against the redox couple Ferrocene/Ferricinium, used as the internal standard

Computational investigation

To shed a better light onto their electronic and excited state properties, complexes **1**–**4** were investigated by means of DFT and TD-DFT calculations. The optimized structures of the complexes are depicted in Figure S22 and the most relevant bond distances and angles are reported in Table S2 of the Supporting information. As for complex **2**, the computed optimized structure could be compared to the experimental one (Figure 2) directly testifying a good agreement for bond lengths and angles. Similar agreement is found when the computed structures of **1** and **3** are compared to the X-ray structures of the related complexes of the family [Ir(C^N)$_2$(acac)] reported elsewhere.[41,43] These findings corroborated the idea that the employed computational strategy is well adapted for the molecules under investigation. Selected valence Kohn-Sham (KS) orbitals involved in the low-lying excited states are represented in Figure 7 and a more expanded version is available in Figure S23.

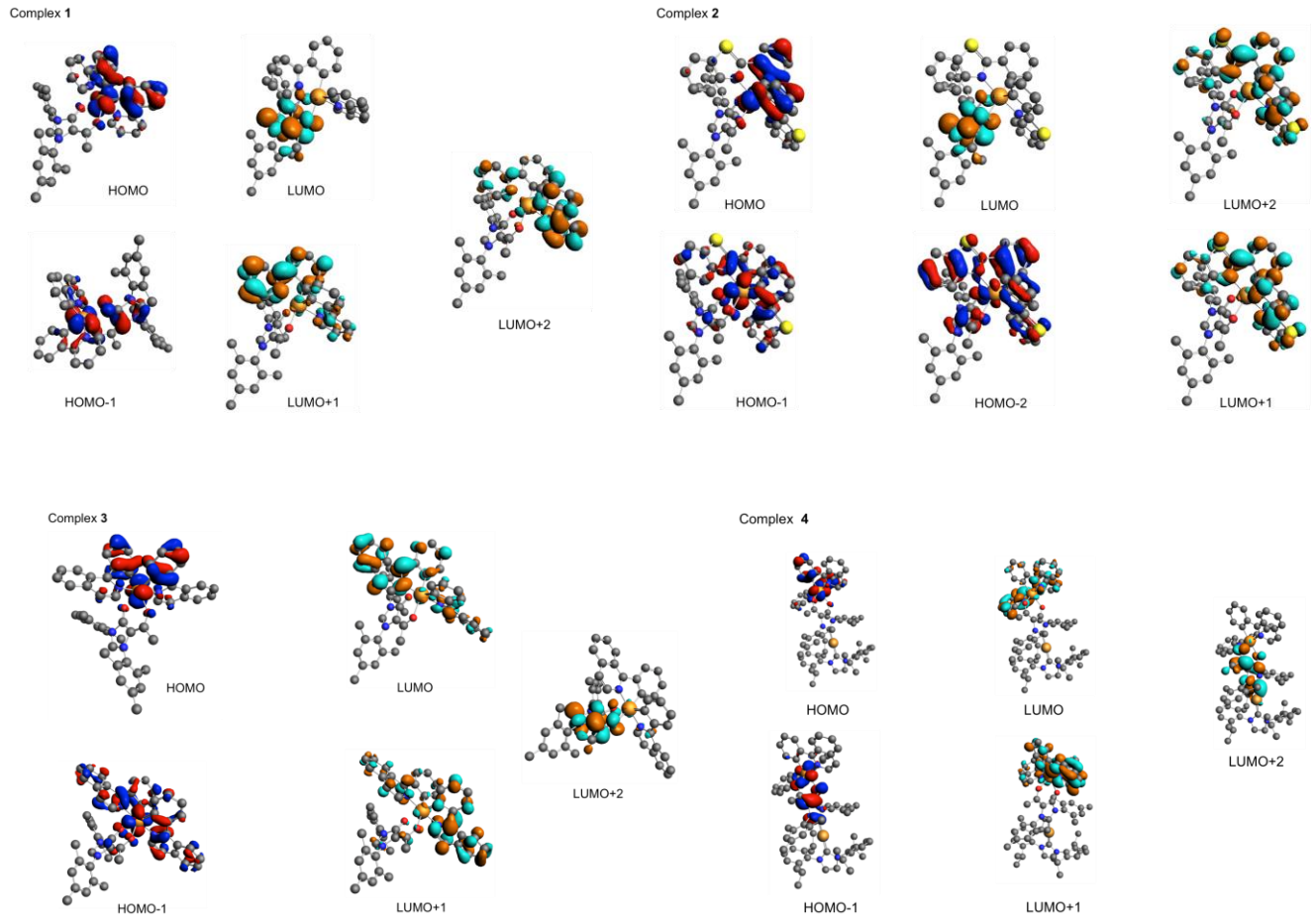

Figure 7. Selected valence KS orbitals involved in low-lying excited states of complexes **1**–**4**. Hydrogen atoms are omitted for sake of clarity.

The HOMO is mainly localized on the C^N ligand and the Ir^{III} center, whereas the LUMO is localized onto the coordinated **IMesAcac**H ligand for complexes **1** and **2**. As far as complex **3** is concerned, the presence of the fused phenyl rings onto the heteroaromatic part of the C^N ligand stabilises the corresponding□□□□□□□□□□orbitals, and the LUMO and

LUMO+1 form a couple of almost degenerate orbitals located onto each of the two isoquinoline moieties; whereas, the empty orbital localized on the **IMesAcac**H scaffold is now the LUMO+2. A similar picture can be drawn for the bimetallic complex **4** for LUMO and LUMO+1; whereas, its LUMO+2 is localized onto the **IMesAcac** fragment of the [**(IPr)Cu(IMesAcac)**] metalloligand.

Within the limit of the single determinant approach and the double-ζ basis sets the KS orbitals are rather localized leading to low-lying excited states of mixed character involving mainly intra-ligand (IL) with metal-to-ligand-charge-transfer (MLCT) and minor ligand-to-ligand-charge-transfer (LLCT) contributions as shown in Figure 8.

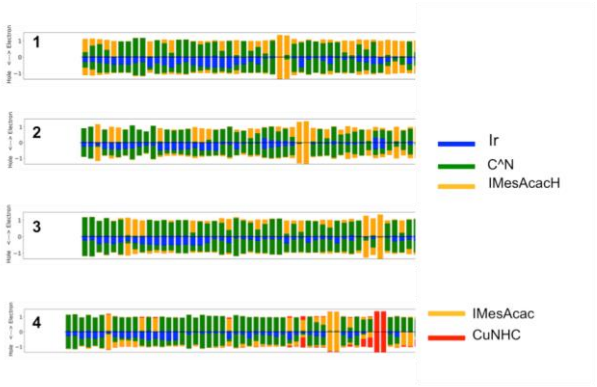

Figure 8. Electron↔hole charge transfer in the low-lying excited states of complexes **1–4**.

The TD-DFT computed absorption spectra with SOC for the three monometallic complexes as well as the hetero-dinuclear species **4** within the UV-visible domain of energy are represented in Figure 9. The corresponding computed spectra without SOC are displayed in Figure S24–S25. The transition energies, oscillator strengths and composition of some selected singlet S_n excited states are reported in Table S3 for complexes **1**–**4** as well as the transition energies to the "spin-orbit" states E_n and related data. The complete set of computed singlet excited states are reported in Table S4, whereas the composition of the low-lying singlet and triplet states of **1–3** and **4** is depicted in Figure 10 and Figure S26, respectively.

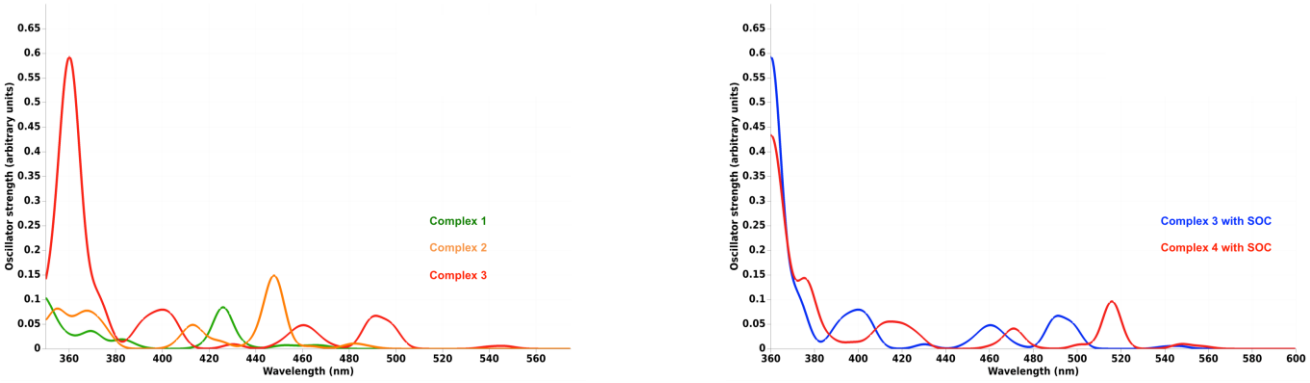

Figure 9. *Left*: Simulated absorption spectra of complexes **1**–**3** with SOC. *Right*: Simulated absorption spectra of complexes **3**–**4** with SOC.

The absorption spectrum of complex **1** is composed of one band at 410 nm of $IL_{C^N}/MLCT_{C^N}$ character (S_2) that bathochromically shifted at 426 nm upon taking into account SOC, which induces S_1/T_2 mixing and a weak absorption between 471–451 nm from the T_1–T_4 triplet states. The large band starting at 389 nm and expanding until 361 nm and beyond is mainly composed of $LLCT_{C^N}$ triplet states (T_5–T_8) with $MLCT_{C^N}/IL_{C^N}$ S_3-S_5 contributions. The upper IL_{C^N} states will give rise to an intense band at 305 nm.

The absorption spectrum of complex **2**, where the pyridine is replaced by a benzothiazole, is very similar to the ppy-based congener. It displays one peak at 431 nm of $IL_{C^N}/MLCT_{C^N}$ character (S_1) shifted to lower energy by SOC, namely at 448 nm. Spin-orbit effects are at the origin of the absorption at 485 nm, the band between 464–442 nm and the shoulder between 425–413 nm. Indeed the first band is composed of the three low-lying singlet (S_1–S_3) states, S_2 ($MLCT_{IMesAcacH}/LLCT_{IMesAcacH}$) and S_3 ($MLCT_{C^N}/IL_{C^N}$) being coupled by SOC to T_4 ($MLCT_{IMesAcacH}/LLCT_{IMesAcacH}$). The shoulder is attributed to S_2

(425 nm) and T_5, T_6 ($MLCT_{C^N}$) coupled by SOC to S_1 and S_3. The weak absorption starting at 372 nm is composed essentially of triplet states (T_7–T_{10}) and S_4 ($MLCT_{IMesAcacH}$). At λ <360 nm the absorption spectrum of complex **2** is constituted mainly of intense IL_{C^N} states. The contribution of the LLCT states is minor in these two complexes.

The substitution of the pyridine by an isoquinoline in complex **3** has important effects on the optical properties. The low-lying singlet states are predominantly $MLCT_{C^N}$ with IL_{C^N} contribution with nearly no charge transfer to the IMesAcacH ligand (Figure 10). The "spin-free" absorption spectrum is blue-shifted with a first band at 395 nm followed by an intense IL_{C^N} peak at 361 nm. The SO effects are rather large with important singlet/triplet mixings that induce a significant bathochromic shift associated to an absorption between 548 nm and 431 nm generated by S_1–S_3/T_3–T_6 SO couplings. The first band at 473–498 nm corresponds to $MLCT_{C^N}$/IL_{C^N} states with major contributions of S_1/T_3 and S_2/T_4 SO mixing. The shoulder at 468–451 nm is assigned mainly to T_3, T_4 $MLCT_{C^N}$/IL_{C^N} and T_5, T_6 $MLCT_{IMesAcacH}$/$LLCT_{IMesAcacH}$ triplet states, T_3 and T_5 being mixed with S_1 and S_3, respectively. The presence of low-lying $MLCT_{C^N}$ and $MLCT_{IMesAcacH}$ states is responsible of these sizeable SO effects in **3**. The upper part of the "spin-orbit" absorption spectrum of complex **3**, beyond 400 nm, traces out the "spin-free" one with predominant IL_{C^N} contributions.

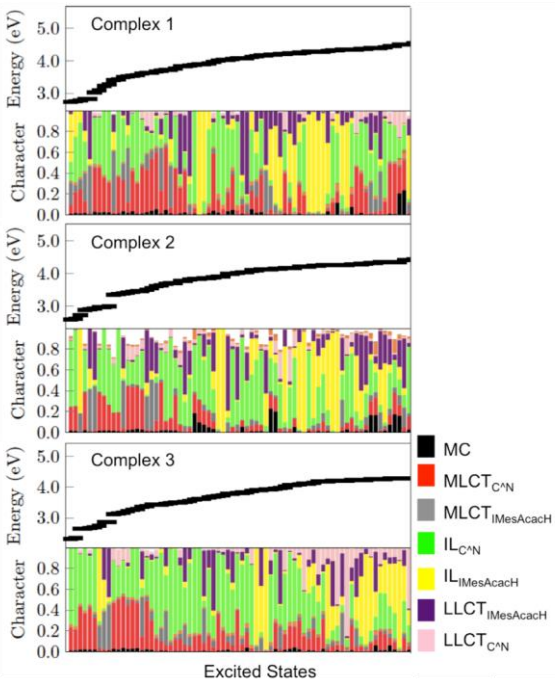

Figure 10. Composition of the low-lying triplet and singlet excited states of complexes **1**–**3** in terms of MC, MLCT, LMCT, LC and LLCT character.

The absorption spectra of complex **3** and complex **4**, its bimetallic analog with a Cu center, are very similar as illustrated by Figure 8 and the results reported in Table S3–S4 in agreement with the experimental features (Figure 2, left box). We observe an important bathochromic shift of the lowest band by 89 nm due to a stabilization of the $MLCT_{C^N}$ states increasing their participation in the low-lying mixed IL_{C^N}/$MLCT_{C^N}$ states of complex **4** as compared to complex **3**. SOC effects mainly operating on the $MLCT_{C^N}$ contributions reduce this bathochromic shift to 19 nm.

As it can be drawn by the results reported in Table 3, the character of the low-lying potentially emissive triplet states may be modified upon structure relaxation. Both T_1 and T_2 keep their $MLCT_{C^N}$/IL_{C^N} character in complexes **2** and **3**. Instead, T_1 remains $MLCT_{IMesAcacH}$/$LLCT_{IMesAcacH}$ state and T_2 converges to a $LLCT_{IMesAcacH}$/$MLCT_{IMesAcacH}$ state in complex **1**. Both these two latter states are expected to be poorly emissive. Nevertheless, the theoretical wavelengths of emission of **1**, 735, 584, 496 nm match with the experimental spectrum (Figure 2, right box) that starts at about 750 nm (T_1) with a first shoulder around 600 nm (T_2) and an intense emission at 520 nm assigned to T_3 and due to the contribution of the IL_{C^N} state.

The emissive behavior of complexes **2** and **3** is controlled essentially by a low-lying $MLCT_{C^N}$/IL_{C^N}. They are calculated at 582 and 539 nm for T_1 and T_2, respectively and both compare well with the experimental higher-energy maximum centered at 583 in complex **2**. For complex **3**, two potentially emissive low-lying states are calculated at 663 and 622 nm, respectively, and well agree with the two experimental maximum at λ_{em} = 650. Although, it is not possible at this stage to clearly state the origin of the emission spectrum, *i.e.* whether it can be attributed to the computed T_1 or T_2, owing to their similar $MLCT_{C^N}$/IL_{C^N} nature and energy. Similarly, complex **4** possess three low-lying potentially emissive $MLCT_{C^N}$/IL_{C^N} triplet states, the two lowest calculated at 667 nm and 580 nm, the second one accessible without any distortion and slightly blue-shifted as compared to T_2 in complex **3** as observed experimentally. Comparison of the computed emission wavelengths from T_1 states shows a bathochromic shift by 4 nm going from **3** to **4**, in agreement with

the 8 nm shift observed in the experimental spectra. Finally, the distortion energy ΔE_{dist} necessary for reaching the potentially emissive states drastically decreases within the series from complex **1** to **4** following the nuclear flexibility of the compounds with values of 0.10 eV and 0.08 eV for T_1 and T_2 in complex **4**, respectively (Table 3).

Table 3. Potentially emissive low-lying triplet excited states of complexes **1**–**4**: character at FC and after structure optimization, calculated vertical transition energies (in eV), Δ□$_{S□□□}$ electronic ground state-triplet energy gap, emission wavelength $\lambda^{□□□□□}$ (in eV and nm) and distortion energy ΔE_{dist} (in eV).

	Character at Franck-Condon	Vertical transition energy [eV]	Δ□($S_{□}$□□$_{n}$) [eV]	ΔE_{dist} [eV]	$\lambda^{□□□□□}$ [eV]	$\lambda^{□□□□□}$ [nm]	Character after structure optimization in acetone
Complex **1**							
T_1	$MLCT_{IMesAcacH}$ /$LLCT_{IMesAcacH}$	2.74	2.27	0.53	1.70	735	$MLCT_{IMesAcacH}$ /$LLCT_{IMesAcacH}$
T_2	$MLCT_{C^N}$ /IL_{C^N}	2.76	2.44	0.30	2.14	584	$LLCT_{IMesAcacH}$ /$MLCT_{IMesAcacH}$
T_3	$MLCT_{C^N}$ /IL_{C^N} $MLCT_{IMesAcacH}$ /$LLCT_{IMesAcacH}$	2.79	2.63	0.13	2.50	496	$IL_{IMesAcacH}$/ $MLCT_{IMesAcacH}$
T_4	$MLCT_{IMesAcacH}$ /$LLCT_{IMesAcacH}$	2.83	2.64	0.03	2.61	475	$MLCT_{IMesAcacH}$ /$LLCT_{IMesAcacH}$ /$IL_{IMesAcacH}$
T_{14}	$IL_{IMesAcacH}$	3.72					
Complex **2**							
T_1	$MLCT_{C^N}$ /IL_{C^N}	2.59	2.32	0.19	2.13	582	$MLCT_{C^N}$ /IL_{C^N}
T_2	$MLCT_{C^N}$ /IL_{C^N}	2.62	2.41	0.08	2.33	539	$MLCT_{C^N}$ /IL_{C^N}
T_3	$MLCT_{IMesAcacH}$ /$LLCT_{IMesAcacH}$	2.72	2.52	0.11	2.41	514	IL_{C^N} / $MLCT_{C^N}$
T_4	$MLCT_{IMesAcacH}$ /$LLCT_{IMesAcacH}$	2.92	2.56	0.07	2.49	498	$MLCT_{IMesAcacH}$ /$LLCT_{IMesAcacH}$
T_{37}	$IL_{IMesAcacH}$	4.29					
Complex **3**							
T_1	$MLCT_{C^N}$ /IL_{C^N}	2.31	2.06	0.19	1.87	663	$MLCT_{C^N}$ /IL_{C^N}
T_2	$MLCT_{C^N}$ /IL_{C^N}	2.33	2.11	0.10	2.01	622	$MLCT_{C^N}$ /IL_{C^N}
T_3	$MLCT_{C^N}$ /IL_{C^N}	2.66	2.37	0.12	2.25	551	IL_{C^N} /$MLCT_{C^N}$
T_4	$MLCT_{C^N}$ /IL_{C^N}	2.69	2.49	0.04	2.45	506	IL_{C^N}
T_{37}	$IL_{IMesAcacH}$	4.24					
Complex **4**							
T_1	IL_{C^N} / $MLCT_{C^N}$	2.28	1.96	0.10	1.86	667	$MLCT_{C^N}$ /IL_{C^N}

T_2	IL_{C^N} / $MLCT_{C^N}$	2.31	2.22	0.08	2.14	580	$MLCT_{C^N}$ /IL_{C^N}
T_3	$MLCT_{C^N}$ / IL_{C^N}	2.61	-	-	-	-	-
T_4	$MLCT_{C^N}$ /IL_{C^N}	2.64	-	-	-	-	-

Conclusions

Two novel cationic *hetero*bimetallic Ir^{III}/M^{I} complexes, where M^{I} = Cu^{I} and Au^{I}, have been presented that have been prepared straightforwardly by using a stepwise site-selective metalation procedure. The two metal centers are bridged by the hybrid **IMesAcac** ligand, which combines both a chelating acetylacetonato-like and a monodentate diaminocarbene site coordinated onto the Ir^{III} and the M^{I} metal ions, respectively. Both the bimetallic and the monometallic parental species have been thoroughly characterized using chemical, spectroscopical, electrochemical and computational investigation at density functional (DFT) and time-dependent theory (TD-DFT) level, also by introducing SOC effects. The monometallic $[Ir^{III}(C^N)_2(\textbf{IMesAcac}H)]PF_6$ parental species, where C^N = 2-phenyl-pyridine (ppy), 2-phenyl-benzotiazole (2-pbt) and 1-phenylisoquinoline (1-piq), display photoluminescence that is partially quenched by the presence of a close-lying quenching state involving the **IMesAcac**H ancillary ligand in its pro-carbenic form. On the other hand, the bimetallic species bearing the 1-piq ligand display bright red photoluminescence arising from a long-lived excited state ^{3}IL/^{1}MLCT involving the "Ir(1-piq)" fragment. Negligible electronic coupling between the two metal centers is observed in the bimetallic species at their electronic ground state when compared to the monometallic parental complexes, yet the former display reversible electrochemical processes. Nonetheless, the presence of the M^{I} metal ion onto the metalloligand **(IPr)M(IMesAcac)** sizably modifies the electronic properties of the "acac" motif, which increases its donating ability. Thus, upon its coordination onto the Ir^{III} center a slight stabilization of the ^{1}MLCT state occurs in comparison with $[Ir^{III}(1\text{-piq})_2(\textbf{IMesAcac}H)]PF_6$ parental complex. As a noteworthy result, the increased ^{1}MLCT character of the emitting state with admixed ^{3}IL/^{1}MLCT nature yields a two-fold increase of the PLQY and k_r for the bimetallic complexes when compared to the benchmark mononuclear parental complexes. The results herein reported might help for the preparation of phosphorescence bi- and multi-metallic complexes with improved photophysical properties as well as chemical and electrochemical stability suitable for efficient electroluminescent devices emitting in the blue and red region.

Experimental Section

General considerations

All procedures involving iridium complexes were carried out under an argon atmosphere using standard Schlenk techniques. Nuclear magnetic resonance spectra were recorded using a Bruker Avance III HD 500 spectrometer equipped with a N2 cryo-probe CPPBBO Prodigy at 298 K. ^{1}H and ^{13}C NMR spectra were calibrated to residual solvent signals. Elemental analyses were obtained at the AMS Fédération de Chimie Le Bel, University of Strasbourg on a Flash 2000 ThermoFischer Scientific apparatus. HR-ESI-MS spectra were recorded on a MicroToF Bruker equipped with an electrospray ionization source.

Synthesis. The ligand 1-phenyl isoquinoline,[44,50] IMesAcacH,[38] and the chloro-bridged iridium dimers[36] were synthetized accordingly to previously reported methods.

Synthesis of the $Ir(C^N)_2$(IMesAcacH) complexes: general procedure. $[Ir(C^N)_2Cl]_2$ (1.0 eq.) was dissolved in 5 mL of methanol and $AgPF_6$ (2.1 eq) was added. The solution was stirred for 5 hours under argon atmosphere at room temperature. The silver chloride was filtered off and **IMesAcac**H ligand (2.0 eq.) was added to the reaction mixture, which was refluxed overnight. After cooling at room temperature, an aqueous solution of KPF_6 was added and a precipitate was formed. The solid was filtered off and washed carefully with water and diethyl ether.

$[Ir(ppy)_2(\kappa^2\textit{O,O}\text{-IMesAcacH})]PF_6$ (**1**). Yield: 44%. ^{1}H NMR (500 MHz, 298 K, acetone-d_6) δ: 8.94 (s, 1H), 8.68 (d, *J* = 5.0 Hz, 1H), 8.63 (d, *J* = 5.7 Hz, 1H), 8.20 (d, *J* = 7.6 Hz, 2H), 8.10–8.02 (m, 2H), 7.73 (d, *J* = 7.8 Hz, 1H), 7.67 (d, *J* = 7.8 Hz, 1H), 7.42 (dd, *J* = 17.4, 10.9 Hz, 2H), 7.27 (s, 1H), 7.23 (s, 1H), 7.03 (s, 1H), 6.89 (s, 1H), 6.84 (t, *J* = 8.1 Hz, 1H), 6.75 (t, *J* = 8.0 Hz, 1H), 6.67 (t, *J* = 7.5 Hz, 1H), 6.56 (t, *J* = 7.5 Hz, 1H), 6.26 (d, *J* = 7.7 Hz, 1H), 6.02 (d, *J* = 8.5 Hz, 1H), 2.39 (d, *J* = 2.6 Hz, 5H), 2.32 (d, *J* = 1.8 Hz, 5H), 2.21 (s, 3H), 1.64 (s, 2H), 1.53 (s, 2H). ^{13}C NMR (125.77 MHz, 298 K, acetone-d_6) δ 185.1, 168.1, 168.0, 155.7, 148.9, 148.2, 145.3, 144.7, 142.0, 141.4, 141.2, 140.96, 138.8, 138.8, 136.5, 135.6, 135.5, 135.4, 135.2, 133.5, 132.9, 131.4, 130.0, 129.97, 129.5, 129.2, 128.9, 128.8, 127.4, 124.1, 124.0, 122.6, 122.5, 121.7, 121.5, 119.2, 113.4, 28.9, 26.5, 20.2, 20.0, 17.1, 16.6, 15.8. HR-ESI-MS: 863.2959 ([M]$^+$), 863.2934 $[C_{45}H_{42}IrN_4O_2]^+$; elemental analysis calcd for $C_{45}H_{42}F_6IrN_4O_2P{\cdot}2H_2O$: C 51.77, H 4.14, N 5.37; found: C 51.76, H 4.13, N 5.30.

$Ir(2\text{-pbt})_2(\kappa^2\textit{O,O}\text{-IMesAcacH})]PF_6$ (**2**). Yield: 62%. ^{1}H NMR (500 MHz, 298 K, acetone-d_6) δ: 8.89 (s, 1H), 8.34 (d, *J* = 7.9 Hz, 1H), 8.30 (d, *J* = 8.0 Hz, 1H), 8.03 (d, *J* = 8.2 Hz, 1H), 7.84 – 7.78 (m, 2H), 7.74 (d, *J* = 7.7 Hz, 2H), 7.69 – 7.59 (m, 3H), 7.53 (t, *J* = 7.6 Hz, 1H), 7.20 (s, 1H), 7.16 (s, 1H), 7.10 (s, 1H), 6.95 (s, 2H), 6.85 (t, *J* = 7.4 Hz, 1H), 6.72 (t, *J* = 7.4 Hz, 1H), 6.60 (t, *J* = 7.5 Hz, 1H), 6.46 (d, *J* = 7.6 Hz, 1H), 6.23 (d, *J* = 7.7 Hz, 1H), 2.43 (s, 3H), 2.35 (s, 3H), 2.24 (s, 4H), 2.08 (s, 5H), 2.02 (s, 5H), 1.66 (s, 3H), 1.38 (s, 3H). ^{13}C NMR (125.77 MHz, 298 K, acetone-d_6) δ: 186.5, 181.2, 181.1, 156.0, 150.3, 150.0, 142.1, 141.7, 141.5, 141.3, 141.2, 141.2, 136.7, 135.7, 135.3, 135.1, 134.7, 134.5, 131.8, 131.5, 131.1, 130.6, 130.4, 129.98, 129.9, 129.7, 129.4, 128.46, 127.7, 127.1, 126.1, 126.0, 123.9, 123.8, 122.4, 122.4, 118.6, 118.5, 113.6, 28.9, 26.3, 20.2, 20.1, 17.1, 16.4, 16.4, 15.5. HR-ESI-MS: 975.2385 ([M]$^+$), 975.2373 $[C_{49}H_{42}IrN_4O_2S_2]^+$; elemental analysis calcd for $C_{49}H_{42}F_6IrN_4O_2PS_2{\cdot}H_2O$: C 51.71 H 3.90 N 4.92; found: C 48.45 H 3.62 N 4.60.

$Ir(1\text{-piq})_2(\kappa^2\textit{O,O}\text{-IMesAcacH})]PF_6$ (**3**). Yield: 87%. ^{1}H NMR (500 MHz, 298 K, acetone-d_6) δ: 9.17–9.14 (m, 2H), 9.08 – 9.04 (m, 2H), 8.87 (s, 1H), 8.54 (dd, *J* = 12.5, 6.3 Hz, 2H), 8.37 (d, *J* = 8.0 Hz, 1H), 8.24 (d, *J* = 8.0 Hz, 1H), 8.20 (t, *J* = 7.7 Hz, 2H), 7.94 (t, *J* = 9.3 Hz, 5H), 7.87 – 7.81 (m, 3H), 7.26 (s, 1H), 7.19 (s, 1H), 7.01 (s, 1H), 6.97 (d, *J* = 8.1 Hz, 1H), 6.86 (t, *J* = 8.1 Hz, 1H), 6.73 (s, 1H), 6.70 (t, *J* = 6.9 Hz, 1H), 6.59 – 6.52 (m, 3H), 6.14 (d, *J* = 6.9 Hz, 1H), 2.36 (d, *J* = 6.8 Hz, 7H), 2.31 (s, 4H), 2.27 (s, 3H), 2.18

(s, 3H), 1.62 (s, 3H), 1.03 (s, 3H). ^{13}C NMR (125.77 MHz, 298 K, acetone-d_6) δ: 205.2, 185.3, 168.7, 168.5, 155.8, 146.6, 146.1, 146.0, 145.1, 142.0, 140.97, 140.6, 139.97, 137.8, 137.7, 136.4, 135.4, 135.4, 135.3, 135.3, 134.4, 133.5, 131.8, 131.3, 129.99, 129.8, 129.5, 129.1, 128.9, 128.8, 127.8, 127.7, 127.3, 126.5, 126.4, 126.2, 126.2, 121.5, 121.4, 120.9, 120.8, 113.3, 28.9, 26.5, 20.2, 20.0, 17.1, 16.7, 16.6, 15.3. HR-ESI-MS: 963.3258 ($[M]^+$), 963.3248 $[C_{53}H_{46}IrN_4O_2]^+$; elemental analysis calcd for $C_{53}H_{46}F_6IrN_4O_2P•H_2O$: C 55.92 H 4.11 N 4.86; found: C 56.53 H 4.30 N 4.98.

{[Ir(1-piq)$_2$][Cu(IPr)](μ-1κ^2*O,O*:2κ^1*C*-IMesAcac)}PF$_6$ (**4**). Yield: 71%. ^{1}H NMR (500 MHz, 298 K CD_2Cl_2) δ:8.98 (d, *J* = 8.7 Hz, 1H), 8.88 (d, *J* = 7.9 Hz, 1H), 8.26 – 8.19 (m, 2H), 8.11 (d, *J* = 6.3 Hz, 2H), 7.97 (t, *J* = 8.9 Hz, 2H), 7.87 – 7.80 (m, 2H), 7.81 – 7.74 (m, 2H), 7.54 (t, *J* = 7.7 Hz, 2H), 7.43 (d, *J* = 6.0 Hz, 2H), 7.20 (d, *J* = 7.6 Hz, 2H), 7.15 (d, *J* = 7.6 Hz, 2H), 7.04 (s, 2H), 6.95 (t, *J* = 7.4 Hz, 1H), 6.88 (t, *J* = 7.4 Hz, 1H), 6.78 (s, 1H), 6.71 (d, *J* = 14.6 Hz, 1H), 6.66 (t, *J* = 7.3 Hz, 3H), 6.56 (t, *J* = 7.3 Hz, 1H), 6.46 (d, *J* = 7.6 Hz, 1H), 6.37 (s, 1H), 6.08 (d, *J* = 7.5 Hz, 1H), 2.28 (s, 7H), 1.71 (d, *J* = 10.7 Hz, 9H), 1.26 (s, 3H), 1.04 (dd, *J* = 6.6, 3.3 Hz, 12H), 0.83 (d, *J* = 6.9 Hz, 6H), 0.72 (d, *J* = 6.9 Hz, 6H).0.48 (s, 3H); ^{13}C NMR (125.77 MHz, 298 K, CD_2Cl_2) δ: 181.4, 176.9, 169.9, 168.8, 168.4, 147.3, 144.8, 139.7, 137.4, 135.1, 134.8, 134.6, 134.3, 134.1, 133.3, 131.3, 130.5, 130.3, 130.2, 129.95, 129.9, 129.7, 129.4, 129.1, 128.8, 128.3, 127.4, 127.2, 126.6, 126.5, 124.2, 124.2, 123.96, 53.4, 30.6, 29.7, 28.6, 28.5, 25.9, 24.2, 23.9, 23.2, 23.1, 21.0, 17.6, 17.0, 16.9, 15.3. HR-ESI-MS: 1413.5345 ($[M]^+$), 1413.5345 $[C_{80}H_{81}CuIrN_6O_2]^+$; elemental analysis calcd for $C_{80}H_{81}CuF_6IrN_6O_2P$: C 61.62 H 5.24 N 5.39; found: C 60.15 H 5.17 N 5.26.

{[Ir(2-pbt)$_2$][Au(IPr)](μ-1κ^2*O,O*:2κ^1*C*-IMesAcac)}PF$_6$ (**5**). Yield: 49%.^{1}H NMR (500 MHz, 298 K CD_2Cl_2) δ: 9.01 – 8.97 (m, 1H), 8.88 (d, *J* = 7.8 Hz, 1H), 8.23 (dd, *J* = 11.0, 7.2 Hz, 2H), 8.12 (d, *J* = 6.3 Hz, 2H), 7.97 (t, *J* = 7.5 Hz, 2H), 7.88 – 7.80 (m, 2H), 7.80 – 7.74 (m, 2H), 7.53 (t, *J* = 7.7 Hz, 2H), 7.44 (dd, *J* = 6.1, 3.3 Hz, 2H), 7.17 (d, *J* = 7.5 Hz, 2H), 7.13 (d, *J* = 7.7 Hz, 2H), 7.11 (s, 2H), 6.96 (t, *J* = 7.3 Hz, 1H), 6.88 (t, *J* = 7.3 Hz, 1H), 6.78 (s, 1H), 6.72 (s, 1H), 6.70 (s, 1H), 6.67 (t, *J* = 7.4 Hz, 1H), 6.57 (t, *J* = 7.1 Hz, 1H), 6.47 (d, *J* = 7.4 Hz, 1H), 6.37 (s, 1H), 6.09 (d, *J* = 7.4 Hz, 1H), 2.37 (s, 3H), 2.28 (s, *J* = 82.2 Hz, 6H), 1.76 (s, *J* = 17.4 Hz, 3H), 1.72 (d, *J* = 3.9 Hz, 6H),1.26 (s, 2H) 1.07 (d, *J* = 5.2 Hz, 13H), 0.88 (d, *J* = 6.9 Hz, 7H), 0.78 (d, *J* = 6.9 Hz, 6H)., 0.50 (s, 3H). ^{13}C NMR (125.77 MHz, 298 K, CD_2Cl_2) δ: 186.4, 183.96, 181.9, 169.2, 168.8, 158.3, 147.6, 146.9, 146.6, 146.4, 145.4, 145.4, 140.3, 140.1, 139.5, 137.9, 137.7, 135.5, 135.1, 135.1, 134.9, 134.7, 134.6, 133.9, 133.7, 131.8, 131.7, 131.0, 130.5, 130.5, 130.3, 130.2, 129.7, 129.5, 129.2, 128.8, 128.8, 127.8, 127.6, 126.97, 126.9, 126.8, 126.6, 124.4, 124.4, 124.4, 121.7, 121.7, 120.8, 120.4, 114.2, 53.8, 28.9, 26.5, 24.2, 24.1, 23.9, 23.8, 21.6, 21.5, 17.98, 17.4, 17.2, 15.7, 1.2. HR-ESI-MS: 1547.5656 ($[M]^+$), 1547.5724 $[C_{80}H_{81}AuIrN_6O_2]^+$; elemental analysis calcd for $C_{80}H_{81}AuF_6IrN_6O_2P$· 3 CH_2Cl_2: C 51.19 H 4.32 N 4.50; found: C 50.77 H 4.35 N 4.50.

Synthesis of the Gd(IMesAcacH)(NO$_3$)$_3$ complex.

$Gd(NO_3)_3·6H_2O$ (1 equiv.) was dissolved in 3 mL of methanol, **IMesAcac**H (1 equiv.) was added, then the mixture was stirred for 24 hours at room temperature. The precipitate obtained was recrystallized in CH_2Cl_2 that was collected as a white powder (yield 66%). Elemental analysis calcd for $C_{23}H_{26}GdN_5O_{11}$: C, 39.14 H, 3.71 N, 9.92; found C 38.53 H 4.22 N, 9.08

Photophysics

Instrument details. Absorption spectra were measured on a Varian Cary 100 double-beam UV–VIS spectrophotometer and baseline corrected. Steady-state emission spectra were recorded on a Horiba Jobin−Yvon IBH FL-322 Fluorolog 3 spectrometer equipped with a 450 W xenon arc lamp, double-grating excitation, and emission monochromators (2.1 nm mm^{-1} of dispersion; 1200 grooves mm^{-1}) and a Hamamatsu R13456 red sensitive Peltier-cooled PMT detector. Emission and excitation spectra were corrected for source intensity (lamp and grating) and emission spectral response (detector and grating) by standard correction curves. Time-resolved measurements were performed using either the time-correlated single-photon counting (TCSPC) or the Multi Channel Scaling (MCS) electronics option of the TimeHarp 260 board installed on a PicoQuant FluoTime 300 fluorimeter (PicoQuant GmbH, Germany), equipped with a PDL 820 laser pulse driver. A pulsed laser diode LDH-P-C-375 (λ□= 375 nm, pulse full width at half maximum FWHM <50 ps, repetition rate 200 kHz–40 MHz) was used to excite the sample and mounted directly on the sample chamber at 90°. The photons were collected by a PMA Hybrid-07 single photon counting detector. The data were acquired by using the commercially available software EasyTau II (PicoQuant GmbH, Germany), while data analysis was performed using the built-in software FluoFit (PicoQuant GmbH, Germany).

Methods. For time resolved measurements, data fitting was performed by employing the maximum likelihood estimation (MLE) methods and the quality of the fit was assessed by inspection of the reduced χ^2 function and of the weighted residuals. For multi-exponential decays, the intensity, namely I*(t)*, has been assumed to decay as the sum of individual single exponential decays (Eq. 2):

$$I(t) = \sum_{i=1}^{n} \alpha_i exp\left(-\frac{t}{\tau_i}\right) \quad (Eqn. 2)$$

where τ are the decay times and □$_i$ are the amplitude of the component at *t* = 0. In the tables, the percentages to the pre-exponential factors, α_i, are listed upon normalization. Intensity average lifetimes were calculated by using the following equation (Eqn. 3):[51]

$$\bar{\tau} = \frac{a_1\tau_1^2 + a_2\tau_2^2}{a_1\tau_1 + a_2\tau_2} \quad (Eqn. 3)$$

Luminescence quantum yields were measured in optically dilute solutions (optical density <0.1 at the excitation wavelength) and compared to reference emitter by following the method of Demas and Crosby[52] Fluorescein in NaOH 0.1 M (PLQY = 0.92[53] and $Ru(bpy)_3Cl_2$ in air-equilibrated water solution (PLQY = 0.04)[54] were used as reference standards for samples of compounds **1** and **2**–**4**, respectively. All the solvents were spectrophotometric grade. Deaerated samples were prepared by the freeze-pump-thaw technique by using a homemade quartz cuvette equipped with a Rotaflo® stopcock.

Electrochemistry

Anhydrous acetone (Sigma-Aldrich, ACS Reagent plus) and tetra-n-butylammonium hexafluorophosphate ($TBAPF_6$, Fluka, 99%) were used as received. The working electrode was a glassy-carbon disk electrode (2 mm diameter, Princeton Applied Research GO224). The electrode was polished as already described elsewhere.[55] Before experiments, the electrode was further polished with a 0.05 μm polycrystalline diamond suspension (Buehler, MetaDI) and electrochemically activated in the background solution by means of several voltammetric cycles at 0.5 Vs^{-1} between the anodic and the cathodic solvent/electrolyte discharges, until the expected quality features were attained.[56] A platinum wire served as the counter electrode and a silver wire, separated from the main electrolytic compartment by a Vycor® frit, was used as a quasi-reference electrode. At the end of each experiment, its potential was calibrated against the ferricenium/ferrocene couple, used as an internal redox standard. The cyclic voltammetry (CV) and differential pulse voltammetry (DPV) experiments were carried out in acetone/0.1 M $TBAPF_6$ under an Ar atmosphere, using a 1 mM concentration for the electroactive compound. To limit the evaporation of the solvent, a reservoir of acetone was used and connected upstream. The solvent level was frequently checked and rinsed when necessary to avoid any change in the analyte concentration. A CHI 760b Electrochemical Workstation (CH Instruments) was used. For the CV experiments, we employed the feedback correction to minimize the ohmic drop between the working and the reference electrodes.

X-ray diffractometric analysis

The crystals were placed in oil, and a single crystal was selected, mounted on a glass fibre and placed in a low-temperature N_2 stream. X-ray diffraction data collection was carried out on a Bruker PHOTON-III DUO Kappa CPAD diffractometer equipped with an Oxford Cryosystem liquid N2 device, using Mo-Kα radiation (λ = 0.71073 Å). The crystal-detector distance was 37 mm. The cell parameters were determined (APEX3 software)[57] from reflections taken from two sets of 6 frames, each at 10 seconds exposure time. The structure was solved by direct methods using the program SHELXT-2014[58] The refinement and all further calculations were carried out using SHELXL-2014[58] The hydrogen atoms were included at calculated positions and treated as riding atoms using SHELXL default parameters. The non-H atoms were refined anisotropically, using weighted full-matrix least-squares on F^2. A semi-empirical absorption correction was applied using SADABS in APEX3.[57] The SQUEEZE instruction in PLATON[59] was applied. The residual electron density was assigned to two molecules of the acetone solvent. The atoms C(17), C(18), C(19), C(20), C(22), C(23) are disordered over two positions with an occupancy ratio of 0.50/0.50. CCDC 1983127 for complex **2**.

Computational details

The structures of the complexes **1**–**4** in the electronic ground state have been fully optimized at the DFT/B3LYP[60] level of theory using essentially double-ζ basis sets including scalar relativistic effects for all atoms[61]. The use of triple-ζ basis sets does not modify drastically the results obtained for the smallest system, namely complex **1** (systematic ~10 nm red-shift of the singlet transitions). This justifies the use of double-ζ basis sets for the large systems, which could not be handled otherwise. The calculations have been performed in acetone within the COSMO (conductor-like-screening model) model.[62] The absorption spectra have been computed at the TD-DFT level (80 roots for complexes **1**–**3** and 60 roots for complex **4**) including spin-orbit effects at the perturbation level of theory within the zero-order relativistic approximation (ZORA).[63] The structures of the low-lying triplet excited states T_n (n = 1–4) have been optimized at the same level of theory using the Tamm-Dancoff approximation (TDA) in order to avoid triplet instability problems.[64] The calculations have been performed with the ADF *2019* package (ADF, SCM, Theoretical Chemistry, Vrije Universiteit, Amsterdam, The Netherlands https://www.scm.com/doc/ADF/index.html) and the analysis with Theodore http://theodore-qc.sourceforge.net/.

Acknowledgments

A.B. and M.M. kindly acknowledge the Université de Strasbourg and CNRS for financial support. The International Centre for Frontier Research in Chemistry (icFRC), and the Labex CSC (ANR-10-LABX-0026 CSC) within the Investissement d'Avenir program ANR-10-IDEX-0002-02 is also acknowledged for funding the PhD fellowship of A.B.. Dr Lydia Brelot and Corinne Bailly are gratefully acknowledged for X-ray crystallographic analyses.

Keywords: cyclometalating ligand • density functional theory • N-heterocyclic carbene • hybrid ligand • iridium

[1] a) E. Zysman-Colman (Ed.), *Iridium(III) in optoelectronic and photonics applications*, **2017**, Wiley; b) N. Armaroli, H. J. Bolink (Eds.) *Photoluminescent materials and electroluminescent devices*, *Top. Curr. Chem.* **2016**; c) H. Yersin (Ed.), *Highly Efficient OLEDs with Phosphorescent Materials*, Springer, **2008** Wiley-VCH, Weinheim, Germany.

[2] a) T.-Y. Li, J. Wu, Z-G. Wu, Y.-X. Zheng, J. L. Zuo, Y. Pan, *Coord. Chem. Rev.* **2018**, *374*, 55; b) A. F. Henwood, E. Zysman-Colman, *Chem. Commun.* **2017**, *53*, 807; c) D. Ma, T. Tsuboi, Y. Qiu, L. Duan, *Adv. Mater.* **2017**, *29*, 1603253; d) J. Lee, H-F. Chen, T. Batagoda, C. Coburn, P. I. Djurovich, M. E. Thompson, S. R. Forrest, *Nature Mater.* **2016**, *15*, 92; R. Zaen, K. -M. Park, K. H. Lee, J. Y. Lee, Y. Kang, *Adv. Opt. Mater.* **2019**, *7*, 1901387; e) I. Omae, *Coord. Chem. Rev.* **2016**, *310*, 154; f) P. Tao, W-L. Li, J. Zhang, S. Guo, Q. Zhao, H. Wang, B. Wei, S-J. Liu, X-H. Zhou, Q. Yu, B-S. Xu, W. Huang, *Adv. Funct. Mater.* **2016**, *26*, 881; g) R. D. Costa, E. Ortí, H. J. Bolink, F. Monti, G. Accorsi, N. Armaroli, *Angew. Chem. Int. Ed.* **2012**, *51*, 8178; h) C-W. Lu, Y. Wang, Y. Chi, *Chem. Eur. J.* **2016**, *22*, 17892; i) Y. Chi, T-K. Chang, P. Ganesan, P. Rajakannu, *Coord. Chem. Rev.* **2017**, *346*, 91; j) A. Bonfiglio, M. Mauro, *Eur. J. Inorg. Chem.*, *manuscript submitted*.

[3] a) A. J. Howarth, R. Patia, D. L. Davies, F. Lelj, M. O. Wolf, K. Singh, *Eur. J. Inorg. Chem*. **2014**, 3657; b) C. Latouche, D. Skouteris, F. Palazzetti, V. Barone, *J. Chem. Theory Comput.* **2015**, *11*, 3281; c) D. Han, L. Zhao, X. Han, *Photochem. Photobiol. Sci.* **2019**, *18*, 2766; d) B. J. Powell, *Coord. Chem. Rev.* **2015**, *295*, 46; e) H. Brahim, C. Daniel, *Comput. Theor. Chem.* **2014**, *219*, 1040; f) H. Brahim, B. Haddad, M. Boukabene, S. Brahim, B. Ariche, *Comput. Theor. Chem.* **2017**, *8*, 1101; g) H. Brahim, B. Haddad, S. Brahim, A. Guendouzi, *J. Mol. Model.* **2017**, *23*, 344; h) D. Hadji, H. Brahim, *Theor. Chem. Acc.* **2018**, 137.

[4] a) J. H. Van Diemen, R. Hage, J. G. Haasnoot, H. E. B. Lempers, J. Reedijk, J. G. Vos, L. De Cola, F. Barigelletti, V. Balzani, *Inorg. Chem.* **1992**, *31*, 3518; b) G. Denti, S. Campagna, S. Serroni, M. Ciano, V. Balzani, *J. Am. Chem. Soc.* **1992**, *114*, 2944; c) S. Serroni, A. Juris, S. Campagna, M. Venturi, G. Denti, V. Balzani, *J. Am. Chem. Soc.* **1994**, *116*, 9086; d) V. Balzani, A. Juris, M. Venturi, S. Campagna, S. Serroni, *Chem. Rev.* **1996**, *96*, 759; e) L. De Cola, P. Belser, *Coord. Chem. Rev.* **1998**, *177*, 301; f) S. Welter, N. Salluce, P. Belser, M. Groeneveld, L. De Cola, *Coord. Chem. Rev.* **2005**, *249*, 1360; g) M. Gagliardo, G. Rodríguez, H. H. Dam, M. Lutz, A. L. Spek, R. W. A. Havenith, P. Coppo, L. De Cola, F. Hartl, G. P. M. van Klink, G. van Koten, *Inorg. Chem.* **2006**, *45*, 2143; h) A. Barbieri, B. Ventura, R. Ziessel, *Coord. Chem. Rev.* **2012**, *256*, 1732; i) K. J. Arma, J. A. G. Williams, *Dalton Trans*. **2006**, 2172; j) C. Sabatini, A. Barbieri, F. Barigelletti, K. J. Armb, J. A. G. Williams, *Photochem. Photobiol. Sci.* **2007**, *6*, 397.

[5] J. H. Van Diemen, R. Hage, J. G. Haasnoot, H. E. B. Lempers, J. Reedijk, J. G. Vos, L. De Cola, F. Barigelletti, V. Balzani, *Inorg. Chem.* **1992**, *31*, 3518.

[6] a) M. Cavazzini, P. Pastorelli, S. Quici, F. Loiseau, S. Campagna, *Chem. Commun.* **2005**, 5266; b) E. A. Plummer, J. W. Hofstraat, L. De Cola, *Dalton Trans.* **2003**, 2080; c) F. Lafolet, S. Welter, Z. Popovic, L. De Cola, *J. Mater. Chem.* **2005**, *15*, 2820; d) V. L. Whittle, J. A. G. Williams, *Inorg. Chem.* **2008**, *47*, 6596; e) V. L. Whittle, J. A. G. Williams, *Dalton Trans.* **2009**, 3929; f) A. Auffrant, A. Barbieri, F. Barigelletti, J.-P. Collin, L. Flamigni, C. Sabatini, J.-P. Sauvage, *Inorg. Chem.* **2006**, *45*, 10990.

[7] R. D. Costa, G. Fernández, L. Sánchez, N. Martín, E. Ortí, H. J. Bolink, *Chem. Eur. J.* **2010**, *16*, 9855.

[8] F. Neve, A. Crispini, S. Serroni, F. Loiseau, S. Campagna, *Inorg. Chem*. **2001**, *40*, 1093.

[9] A. M. Soliman, D. Fortin, P. D. Harvey, E. Zysman-Colman, *Dalton Trans.* **2012**, *41*, 9382.

[10] a) G. Li, D. G. Congrave, D. Zhu, Z. Su, M. R. Bryce, *Polyhedron* **2018**, *140*, 146.; b) G. Li, D. Zhu, X. Wang, Z. Su, M. R. Bryce, *Chem. Soc. Rev.* **2020**, *49*, 765.

[11] a) S. Bettington, M. Tavasli, M. R. Bryce, A. S. Batsanov, A. L. Thompson, H. A. Al Attar, F. B. Dias, A. P. Monkman, *J. Mater. Chem.* **2006**, *16*, 1046; b) A. M'hamedi, A. S. Batsanov, M. A. Fox, M. R. Bryce, K. Abdullah, H. A. Al-Attar, A. P. Monkman, *J. Mater. Chem.* **2012**, *22*, 13529.

[12] Y. Zheng, A. S. Batsanov, M. A. Fox, H. A. Al-Attar, K. Abdullah, V. Jankus, M. R. Bryce, A. P. Monkman, *Angew. Chem. Int. Ed.* **2014**, *53*, 11616.

[13] D. G. Congrave, Y-T. Hsu , A. S. Batsanov , A. Beeby, M. R. Bryce, *Dalton Trans.* **2018**, *47*, 2086.

[14] D. G. Congrave, A. S. Batsanov, M. R. Bryce, *Dalton Trans.*, **2018**, *47*, 16524.

[15] A. M'hamedi, M. A. Fox, A. S. Batsanov, H. A. Al-Attar, A. P. Monkman, M. R. Bryce, *J. Mater. Chem. C* **2017**, *5*, 6777.

[16] Y-B. Gong, P. Zhang, Y-R. Gu, J.-Q. Wang, M.-M. Han, C. Chen, X.-J. Zhan, Z.-L. Xie, B. Zou, Q. Peng, Z.-G. Chi, Z. Li, *Adv. Opt. Mater.* **2018**, *6*, 1800198.

[17] a) R. E. Daniels, S. Culham, M. Hunter, M. C. Durrant, M. R. Probert, W. Clegg, J. A. G. Williams, V. N. Kozhevnikov, *Dalton Trans.* **2016**, *45*, 6949; b) M. Z. Shafikov, R. Daniels, V. N. Kozhevnikov, *J. Phys. Chem. Lett.* **2019**, *10*, 7015.

[18] a) P-H. Lanoë, C. M. Tong, R. W. Harrington, M. R. Probert, W. Clegg, J. A. G. Williams, V. N. Kozhevnikov, *Chem. Commun.* **2014**, *50*, 6831; b) V. N. Kozhevnikov *ECS J. Solid. State Sci. Tech*. **2019**, *8*, R84.

[19] a) X. Yang, X. Xu, J-S. Dang, G. Zhou, C-L Ho, W-Y. Wong, *Inorg. Chem.* **2016**, *55*, 1720; b) X. Yang, Z. Feng, J. Zhao, J-S. Dang, B. Liu, K. Zhang, G. Zhou, *ACS Appl. Mater. Interfaces*, **2016**, *8*, 33874.

[20] V. N. Kozhevnikov, M. C. Durrant, J. A. G. Williams, *Inorg. Chem*. **2011**, *50*, 6304.

[21] G. Turnbull, J. A. G. Williams, V.N. Kozhevnikov, *Chem. Comm.* **2017**, *53*, 2729.

[22] M. Z. Shafikov, S. Tang, C. Larsen, M. Bodensteiner, V. N. Kozhevnikov, L. Edman, *J. Mater. Chem. C* **2019**, *7*, 10672.

[23] R. Muñoz-Rodríguez, E. Buñuel, N. Fuentes, J. A. G. Williams, D. J. Cárdenas, *Dalton Trans.* **2015**, *44*, 8394.

[24] a) D. Bourissou, O. Guerret, F. P. Gabbaï, G. Bertrand, Chem. Rev. **2000**, *100*, 39; b) M. N. Hopkinson, C. Richter, M. Schedler, F. Glorius, *Nature* **2014**, *510*, 485; c) S. P. Nolan, in *N-Heterocyclic Carbenes in Synthesis*; Wiley-VCH: Weinheim, Germany, **2006**; d) S. Diez-Gonzalez (Ed.) in *N-Heterocyclic Carbenes: From Laboratory Curiosities to Efficient Synthetic Tools*, 2nd edition, RSC Publishing, London, **2016.**

[25] a) H. V. Huynh, *Chem. Rev.* **2018**, *118*, 9457; b) A. Gomez-Suarez, D. J. Nelson, S. P. Nolan, *Chem. Commun.* **2017**, *53*, 2650; c) L. Benhamou, E. Chardon, G. Lavigne, S. Bellemin-Laponnaz, V. César, *Chem. Rev.* **2011**, *111*, 2705; d) V. César, S. Bellemin-Laponnaz, L. H. Gade, *Chem. Soc. Rev.* **2004**, *33*, 619.

[26] a) E. Peris; *Chem. Rev.* **2018**, *118*, 9988; b) D. Janssen-Muller, C. Schlepphorst, F. Glorius, *Chem. Soc. Rev.* **2017**, *46*, 4845 ; c) O. M. Ogba, N. C. Warner, D. J. O'Leary, R. H. Grubbs, *Chem. Soc. Rev*. **2018**, *47*, 4510; d) R. D. J. Froese, C. Lombardi, M. Pompeo, R. P. Rucker, M. G. Organ, *Acc. Chem. Res.* **2017**, *50*, 2244; e) A. A. Danopoulos, T. Simler, P. Braunstein, *Chem. Rev.* **2019**, *119*, 3730; f) S. Bellemin-Laponnaz, S. Dagorne, *Chem. Rev.* **2014**, *114*, 8747.

[27] R. Visbal, M. Concepcion Gimeno, *Chem. Soc. Rev.* **2014**, *43*, 3551.

[28] a) C. A. Smith, M. R. Narouz, P. A. Lummis, I. Singh, A. Nazemi, C-H. Li, C. M. Crudden, *Chem. Rev.* **2019**, *119*, 4986; b) A. V. Zhukhovitskiy, M. J. MacLeod, J. A. Johnson, *Chem. Rev.* **2015**, *115*, 11503.

[29] a) L. Mercs, A. Neels, H. Stoeckli-Evans, M. Albrecht, *Inorg. Chem.* **2011**, *50*, 8188; b) M. Nussbaum, O. Schuster, M. Albrecht, *Chem. Eur. J.* **2013**, *19*, 17517.

[30] J. A. Mata, F. E. Hahn, E. Peris, *Chem. Sci.* **2014**, *5*, 1723.

[31] L. Mercs, M. Albrecht, *Chem. Soc. Rev.* **2010**, *39*, 1903.

[32] A. G. Tennyson, E. L. Rosen, M. S. Collins, V. M. Lynch, C. W. Bielawski, *Inorg. Chem.* **2009**, *48*, 6924.

[33] S. Gonell, M. Poyatos, E. Peris, *Chem. Eur. J.* **2014**, *20*, 9716

[34] S. Ibáñez, A. Guerrero, M. Poyatos, E. Peris, *Chem. Eur. J.* **2015**, *21*, 10566.

[35] V. César, V. Mallardo, A. Nano, G. Dahm, N. Lugan, G. Lavigne, S. Bellemin-Laponnaz, *Chem. Comm.* **2015**, *51*, 5371.

[36] M. Nonoyama, *Bull. Chem. Soc. Jpn.* **1974**, *47*, 767.

[37] P. Coppo, E. A. Plummer, L. De Cola, *Chem. Commun*. **2004**, 1774.

[38] V. César, V. Mallardo, A. Nano, S. F. DePeter, S. Bastin, A. Sournia-Saquet, A. Maisse-François, N. Lugan, S. Bellemin-Laponnaz, *ACS Omega* **2018***, 3,* 15582.

[39] J. Dai, K. Zhou, M. Li, H. Sun, Y. Chen, S. Su, X. Pu, Y. Huang, Z. Lu, *Dalton Trans.* **2013**, *42*, 10559.

[40] a) J. V. Caspar, T. J. Meyer, *J. Phys. Chem.* **1983**, *87*, 952; b) E. M. Kober, J. V. Caspar, R. S. Lumpkin, T. J. Meyer, *J. Phys. Chem.* **1986**, *90*, 3722.

[41] S. Lamansky, P. Djurovich, D. Murphy, F. Abdel-Razzaq, H.-E. Lee, C. Adachi, P. E. Burrows, S. R. Forrest, M. E. Thompson, *J. Am. Chem. Soc.* **2001**, *123*, 4304.

[42] a) H. Yersin, A. F. Rausch, R. Czerwieniec, T. Hofbeck, T. Fischer, *Coord. Chem. Rev.* **2011**, *255*, 2622; b) A. F. Rausch, H. H. H. Homeier, P. I. Djurovich, Mark E. Thompson, H. Yersin, Proc. SPIE 6655, *Organic Light Emitting Materials and Devices XI*, 66550F, **2007.**

[43] S. Lamansky, P. Djurovich, D. Murphy, F. Abdel-Razzaq, R. Kwong, I. Tsyba, M. Bortz, B. Mui, R. Bau, M. E. Thompson, *Inorg. Chem.* **2001**, *40*, 1704.

[44] Y.-J. Su, H.-L. Huang, C.-L. Li, C.-H. Chien, Y.-T. Tao, P.-T. Chou, S. Datta, R.-S. Liu, *Adv. Mater.* **2003**, *15*, 884.

[45] a) P. J. J. Hay, *Phys. Chem. A* **2002**, *106*, 1634; b) J. Li, P. I. Djurovich, B. D. Alleyne, M. Yousufuddin, N. N. Ho, J. C. Thomas, J. C. Peters, R. Bau, M. E. Thompson, *Inorg. Chem.* **2005**, *44*, 1713.

[46] Y. Chen, G. Cheng, K. Li, D. P. Shelar, W. Lu, C.-M. Che, *Chem. Sci.* **2014**, *5*, 1348.

[47] H. Yersin, A. F. Rausch, R. Czerwieniec, T. Hofbeck, T. Fischer, *Coord. Chem. Rev.* **2011**, *255*, 2622.

[48] A. Kapturkiewicz, J. Nowacki, P. Borowicz, *Electrochim. Acta* **2005**, *50*, 3395.

[49] A. J. Bard, L. R. Faulkner in *Electrochemical Methods: Fundamentals and Applications*, 2nd Ed. **2000**, Wiley.

[50] N. Miyaura, A. Suzuki, *J. Chem. Soc. Chem. Commun.* **1979**, 866.

[51] J. R. Lakowicz in *Principles of Fluorescence Spectroscopy*, Springer, 3rd Ed., New York, **2006**, 141.

[52] a) G. A. Crosby, J. N. C. Demas, *J. Am. Chem. Soc.* **1970**, *92*, 7262; b) H. Ishida, J.-C. Bünzli, A. Beeby, *Pure Appl. Chem*. **2016**, *88*, 701; c) C. Würth, M. Grabolle, J. Pauli, M. Spieles, U. Resch-Genger, *Nat. Prot.* **2013**, *8*, 1515.

[53] a) A. M. Brouwer, *Pure Appl. Chem.* **2011**, *83*, 2213; b) L. Porrès, A. Holland, L. O. Palsson, A. P. Monkman, C. Kemp, A. Beeby. *J. Fluoresc.* **2006**, *16*, 267.

[54] I. Ishida, S. Tobita, Y. Hasegawa, R. Katoh, K. Nozaki, *Coord. Chem. Rev.* **2010**, *254*, 2449.

[55] S. Antonello, M. Musumeci, D. D. M. Wayner, F. Maran, *J. Am. Chem.Soc.* **1997**, *119*, 9541.

[56] A. Belèn-Meneses, S. Antonello, M. C. Arévalo, F. Maran, *Electroanalysis* **2006**, *18*, 363.

[57] *M86-EXX229V1 APEX3 User Manual*, Bruker AXS Inc. Madison, USA, **2016.**

[58] G. M. Sheldrick, *Acta Cryst.* **2015**, *A71*, 3.

[59] A.L. Spek, *Acta Cryst.* **2015**, *C71*, 9.

[60] P. J. Stephens, F. J. Devlin, C.F. Chabalowski, M. J. Frisch, *J. Phys. Chem.* **1994**, *98*, 11623.

[61] E. Van Lenthe, E. J. Baerends, *J. Comput. Chem.* **2002**, *24*, 1142.

[62] A. Klamt, *J. Phys. Chem.* **1995**, *99*, 2224.

[63] a) E. van Lenthe, R. van leeuwen, E. J. Baerends, J. G. Snijders, *Int. J. Quant. Chem.* **1996**, *57*, 281; b) F. Wang, T. Ziegler, *J. Chem. Phys.* **2005**, *123*, 154102; c) F. Wang, T. Ziegler, E. van Lenthe, S. van Gisbergen, E. J. Baerends, *J. Chem. Phys.* **2005**, *122*, 204103.

[64] M. J. G. Peach, D. J. Tozer, *J. Phys. Chem. A.* **2012**, *116*, 9783.